The oceanic crustal structure at the extinct, slow to ultraslow Labrador Sea spreading center

Matthias Delescluse, Thomas Funck, Sonya A. Dehler, Keith E. Louden, Louise Watremez

RESEARCH ARTICLE

Key Points:
- Seismic refraction images the thin crust of the Labrador Sea spreading ridge
- Faulting becomes dominant as spreading rate decreases toward ridge extinction
- Extreme thinning of the crust as well as an oceanic core complex are observed

Correspondence to:
M. Delescluse,
delescluse@geologie.ens.fr

The oceanic crustal structure at the extinct, slow to ultraslow Labrador Sea spreading center

Matthias Delescluse[1], Thomas Funck[2], Sonya A. Dehler[3], Keith E. Louden[4], and Louise Watremez[4,5]

[1]Laboratoire de Géologie de l'ENS-PSL Research University-CNRS UMR 8538, Paris, France, [2]Geological Survey of Denmark and Greenland, Copenhagen, Denmark, [3]Geological Survey of Canada, Dartmouth, Nova Scotia, Canada, [4]Department of Oceanography, Dalhousie University, Halifax, Nova Scotia, Canada, [5]National Oceanography Centre Southampton, University of Southampton, Southampton, UK

Abstract Two seismic refraction lines were acquired along and across the extinct Labrador Sea spreading center during the Seismic Investigations off Greenland, Newfoundland and Labrador 2009 cruise. We derived two *P* wave velocity models using both forward modeling (RAYINVR) and traveltime tomography inversion (Tomo2D) with good ray coverage down to the mantle. Slow-spreading Paleocene oceanic crust has a thickness of 5 km, while the Eocene crust created by ultraslow spreading is as thin as 3.5 km. The upper crustal velocity is affected by fracturation due to a dominant tectonic extension during the waning stage of spreading, with a velocity drop of 0.5 to 1 km/s when compared to Paleocene upper crustal velocities (5.2–6.0 km/s). The overall crustal structure is similar to active ultraslow-spreading centers like the Mohns Ridge or the South West Indian Ridge with lower crustal velocities of 6.0–7.0 km/s. An oceanic core complex is imaged on a 50 km long segment of the ridge perpendicular line with serpentinized peridotites (7.3–7.9 km/s) found 1.5 km below the basement. The second, ridge-parallel line also shows extremely thin crust in the extinct axial valley, where 8 km/s mantle velocity is imaged just 1.5 km below the basement. This thin crust is interpreted as crust formed by ultraslow spreading, which was thinned by tectonic extension.

1. Introduction

The Labrador Sea separates Labrador from Southeast Greenland. Initial rifting began in the Cretaceous [*Watt*, 1969; *Srivastava*, 1978]. The north of the Labrador Sea is bounded by volcanic margins [*Keen et al.*, 2012], with the presence of seaward dipping reflectors [*Chalmers and Laursen*, 1995], as is the case farther to the north at the Davis Strait and southern Baffin Bay margins, where high-velocity lower crustal layers are present [*Funck et al.*, 2007]. The area of interest in this study, the south-central Labrador Sea basin, is bounded by asymmetric nonvolcanic continental margins with the Greenland continental margin [*Chian and Louden*, 1994] being much narrower than the Labrador margin [*Chian and Louden*, 1995]. Magnetic anomalies [*Roest and Srivastava*, 1989; *Chalmers and Laursen*, 1995; *Oakey and Chalmers*, 2012] and Ocean Drilling Program wells [*Srivastava et al.*, 1989] constrain the oceanic spreading history. There is an agreement that spreading started no later than Chron C27 [*Chalmers and Laursen*, 1995; *Oakey and Chalmers*, 2012] in the Paleocene. However, some authors [*Roest and Srivastava*, 1989; *Srivastava and Roest*, 1999] have suggested that oceanic spreading may have started as early as Chron C33. This debate is difficult to resolve because the proposed Cretaceous anomalies do not lie above a typical oceanic crustal structure [*Chalmers and Laursen*, 1995] but rather above a transitional crust with possible serpentinization of the mantle [*Chian and Louden*, 1995]. The Paleocene magnetic anomalies (C27 to C25) are perpendicular to the NE-SW oriented opening direction between Greenland and North America and indicate slow spreading rates. Spreading segments are offset by transform faults such as the Cartwright-Julianehaab Fracture Zone (Figure 1). Between Chron C25 and C24 (late Paleocene, early Eocene), plate reorganizations occur following separation of Greenland from Eurasia and the opening of the Northeast Atlantic, in possible connection with the migration of the Icelandic plume head from West Greenland toward its present-day position [*Lawver and Müller*, 1994; *Storey et al.*, 1998]. Greenland then moved northward with respect to North America, and spreading in the Eocene became oblique and ultraslow [*Roest and Srivastava*, 1989] until the waning stage of accretion and the extinction of spreading around Chron C13 (latest Eocene) [*Srivastava*, 1978].
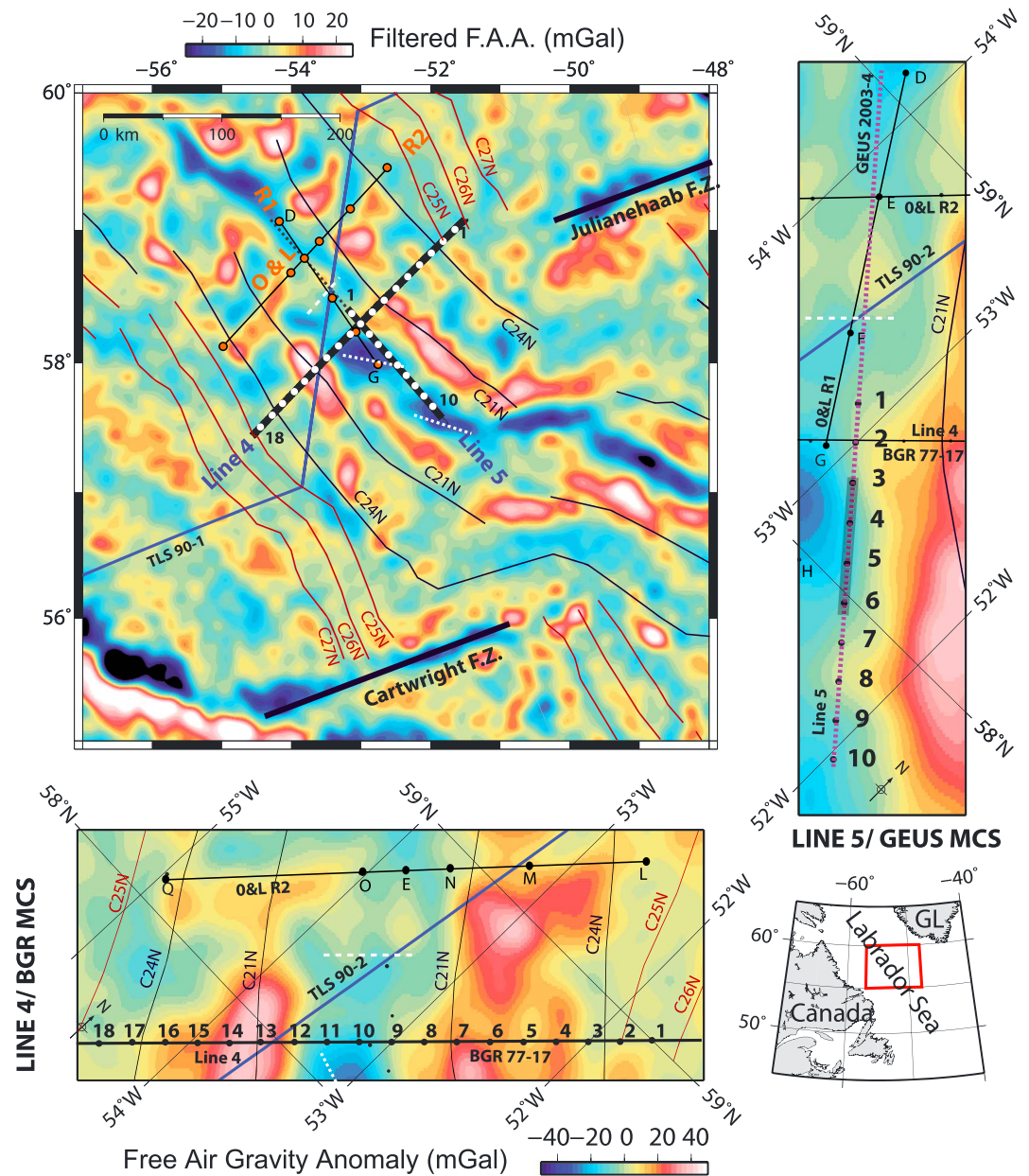
Figure 1. The extinct Labrador Sea spreading center. (top left) The background of the main map displays filtered (<100 km) satellite free air gravity anomalies (FAA) from the DTU10 grid [*Andersen et al.*, 2010]. White circles represent ocean bottom seismometer (OBS) stations from the SIGNAL (Seismic Investigations off Greenland, Newfoundland and Labrador) experiment, while orange ones are OBS locations of a previous study along Lines R1 and R2 [*Osler and Louden*, 1992, 1995]. (top right and bottom left) Blowups of both SIGNAL lines are displayed with an unfiltered satellite F.A.A background, and station numbers of OBS. SIGNAL Line 4 coincide with seismic Line BGR 77-17 [*Hinz et al.*, 1979; *Chalmers and Laursen*, 1995], while SIGNAL Line 5 follows the GEUS 2003-4 seismic line (dashed). The blue lines are seismic profiles TLS 90-1, TLS 90-2, and TLS 90-3 (from west to east, see *Srivastava and Keen* [1995]). Magnetic anomalies are from *Roest and Srivastava* [1989]. White dashed lines are interpreted spreading subsegments and transform fault (compare with Figure 15). Thick solid black lines represent major fracture zones (FZ). GL: Greenland.

Studying the Labrador Sea oceanic crustal structure addresses many important processes from ultraslow-spreading regimes to spreading ridge extinction. First, among the extinct spreading centers (Southeast-Pacific, Labrador Sea/Baffin Bay, Aegir Ridge, Wharton Basin, South China Sea, Shikoku Basin, Galapagos Rise, Philippine Sea, Caroline Sea, Scotia Sea, and Tasman Sea [*Bouysse et al.*, 2010]), only the Labrador Sea [*Osler and Louden*, 1992], Aegir Ridge [*Grevemeyer et al.*, 1997; *Breivik et al.*, 2006], Baffin Bay [*Funck et al.*, 2012;

Suckro et al., 2012], and the Shikoku back-arc basin [*Nishizawa et al.*, 2011] have been sampled by seismic refraction data. The processes leading to the extinction of seafloor spreading are not well known, particularly regarding the balance between volcanism and tectonism. Previous studies show significant normal faulting across the Labrador Sea extinct spreading center [*Osler and Louden*, 1992, 1995; *Srivastava and Keen*, 1995] and the Aegir Ridge [*Uenzelmann-Neben et al.*, 1992; *Grevemeyer et al.*, 1997; *Breivik et al.*, 2006], but thick crust is imaged in Baffin Bay [*Funck et al.*, 2012; *Suckro et al.*, 2012] and the Shikoku Basin [*Nishizawa et al.*, 2011].

In addition, the extinct Labrador Sea spreading center is another example of an ultraslow-spreading system, along with present-day examples from the South West Indian Ridge (SWIR) [*McKenzie and Sclater*, 1971; *Patriat et al.*, 1997] in the Indian Ocean, the Mohns Ridge [*Klingelhöfer et al.*, 2000], the Knipovich Ridge [*Lundin and Doré*, 2002], the Molloy Ridge, and the Gakkel Ridge [*Ehlers and Jokat*, 2009] in the Northeast Atlantic and Arctic Oceans. While the crustal structures of the active ultraslow-spreading ridges have been imaged by seismic refraction data [*Klingelhöfer et al.*, 2000; *Minshull et al.*, 2006; *Jokat et al.*, 2003; *Jokat and Schmidt-Aursch*, 2007], the profiles were acquired with a wide spacing of seismic receivers (OBS, ocean bottom seismometers). Some studies suggest that ultraslow-spreading systems form thinner oceanic crust [*Reid and Jackson*, 1981; *Dick et al.*, 2003], but because very large variations in melt supply are possible at these spreading rates, there is no clear relationship between crustal thickness and spreading rate. Indeed, the refraction results and dredging show large variations in the crustal structure and thickness of ultraslow ridges [*Michael et al.*, 2003]. More work is needed to understand what factors control the "ultraslow" crustal structure. The extinct Labrador Sea rift is characterized by a gradual decrease in spreading rate. With a moderate profile length, the evolution of the crustal structure from slow to ultraslow spreading can be imaged in the same geodynamical framework.

Finally, when spreading becomes magma starved, the crustal structure may be similar to transitional crust at continental margins. As noticed by *Minshull* [2009], ultraslow-spreading ridges are not sufficiently well sampled, and only in areas close to the spreading center, so that a comparison between crustal velocity structures is not very conclusive. As the continent-ocean transition zones sometimes record weak magnetic anomalies [*Srivastava et al.*, 2000; *Sibuet et al.*, 2007], it is not easy to discriminate between extremely thinned continental crust and very slow, almost amagmatic oceanic accretion just after rifting [*Funck et al.*, 2003]. As a result, a better imaging of the thin Labrador Sea oceanic crust [*Srivastava and Keen*, 1995; *Louden et al.*, 1996] may help to better understand late rifting processes such as the transitional crust at the SW Greenland margin [*Chalmers and Laursen*, 1995; *Srivastava and Roest*, 1999].

In this paper, we first present the seismic refraction data set acquired during the SIGNAL 2009 cruise (Seismic Investigations off Greenland, Newfoundland and Labrador) [*Funck et al.*, 2009]. Then we describe the modeling strategy and finally discuss the results in terms of crustal structure, with a particular focus on what happened during plate reorganizations between Chrons C24 and C25 and at Chron C13.

2. Data

2.1. Data Acquisition

In this study, we present two seismic refraction lines (Lines 4 and 5) acquired in 2009 during the SIGNAL cruise (Seismic Investigations off Greenland, Newfoundland and Labrador) onboard CCGS Hudson. Located in the vicinity of a previous experiment targeting the extinct Labrador Sea spreading center [*Osler and Louden*, 1992, 1995, Lines R1 and R2 from Figure 1], both lines were designed to improve the seismic resolution across and along the extinct spreading axis. The 270 km long Line 4 is located across the ridge axis and parallel to Line R2. A total of 18 OBS were deployed along the profile. Line 5 is 144 km long and is located along the ridge axis. Here 10 OBS were deployed. The instrument spacing varies between 12 and 14 km. The air gun array was composed of 12 × 8.4 L G-guns with a total volume of 100 L (6144 cu in.). Shots were time triggered every minute, corresponding to ~150 m distance at a cruise speed of 5 knots (1 knot = 0.5 m/s = 1.85 km/h). Each OBS was equipped with a hydrophone and a three-component geophone deployed directly on the seafloor for improved ground coupling. Data were retrieved from all deployed instruments. Linear clock-drift corrections were applied to synchronize the OBS clocks with the GPS time used to trigger the shots. Only the data from OBS 6 on Line 4 could not be used because of unknown clock-related problems. Positions of the OBS were calculated to correct for their drift during the descent to the seafloor. These relocations were performed using the traveltimes of the water wave arrivals.
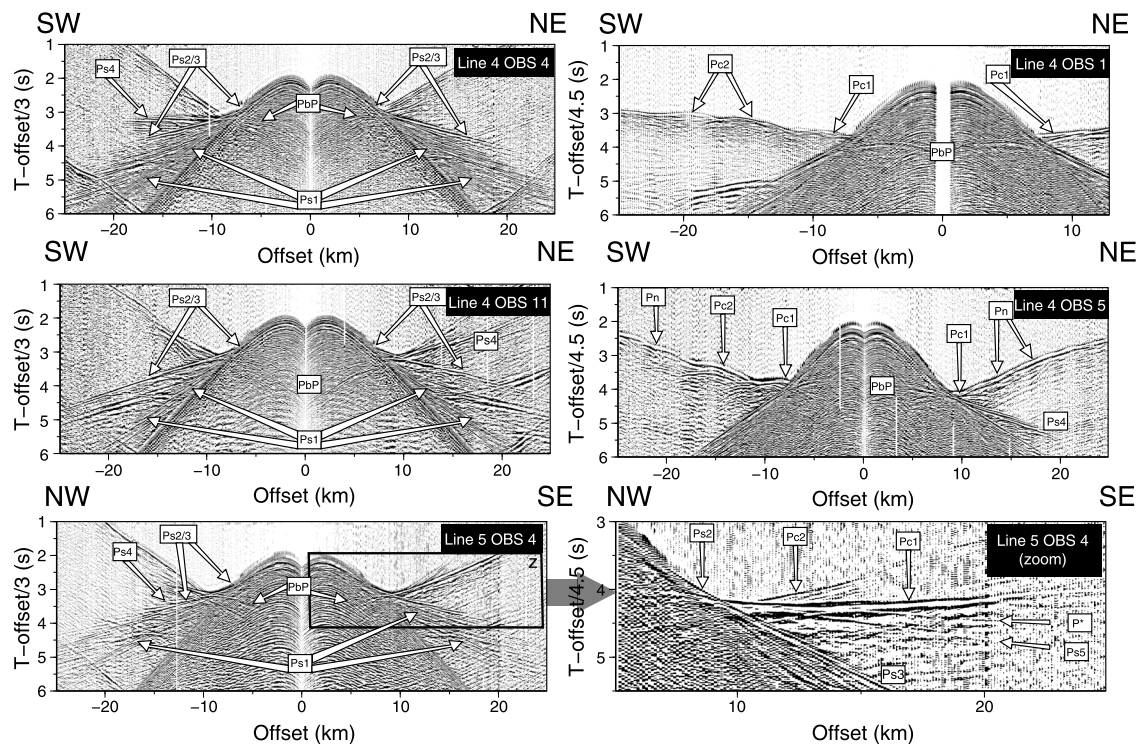
Figure 2. OBS data: sedimentary and crustal arrivals as discussed in the text. The data are band-pass filtered (6–35 Hz) and a predictive deconvolution is applied. Line 4 OBS 4 and Line 4 OBS 11 are records from the hydrophone channels, while all other records are from the vertical geophone channel. The left column uses a reduction velocity of 3 km/s to focus the display on sedimentary arrivals, while the right column uses a reduction velocity of 4.5 km/s, to focus the display on upper crustal arrivals. Phases P_{s5} and P* on Line 5 OBS 4 have slopes indicated by the two arrows. A blow-up of the Line 4 OBS 4 reflections, including the PxP phase is available in supplementary material Figure S1.

2.2. Sedimentary Arrivals and Basement

The overall quality of the data set is good (Figures 2 and 3). Three refraction phases are common to all OBS (P_{s1}, P_{s2}, and P_{s3} phases) with apparent velocities of 1.8 km/s, 2.2 km/s, and 2.4 km/s, respectively (Figures 2 and 3). These arrivals correspond to the regional 2 km thick sediment infill of the Labrador Sea basin (Figure 4). Figure 2 also shows a fourth sedimentary phase (P_{s4}) on some OBS, with apparent velocities ranging from 3.0 km/s to 3.6 km/s. This phase is only recorded on OBSs located above or near the edges of deeper sedimentary basins (units 4A, 4B, and 4C on Figure 4) and only for shots allowing seismic rays to cross these basins. Like phases P_{s1}, P_{s2}, and P_{s3}, phase P_{s4} is also recorded on Line 5, which crosses Line 4 within basin 4A (OBS 9 on Line 4, see Figures 1 and 4). Basement reflections (PbP, Figure 2) are visible on most records, in particular, on the hydrophone channels. An even deeper, unidentified reflection is recorded on OBS 4 on Line 4 (PxP, Figure S1 in the supporting information).

A fifth sedimentary arrival (P_{s5}) is recorded on Line 5 (OBS 3, OBS 4 on Figure 2, and OBS 5). The apparent velocity of this phase is 3.8 km/s. These three OBS also recorded another phase with an apparent velocity of 4 km/s (labeled P*, Figure 2). With such a high apparent velocity, it is probably associated with the upper crustal layer. However, the seismic facies of the corresponding unit on the seismic reflection record (Figure 4) shows slightly tilted interbedded reflectors similar to sediment reflectors, although characterized by lower frequencies. Acoustic basement lies just below these low-frequency reflectors.

2.3. Crustal and Mantle Arrivals

Most of the seismic phases described so far are secondary arrivals. The upper crustal refraction (P_{c1}) is sometimes a first arrival, sometimes a secondary arrival. The apparent velocity of the P_{c1} phase is ~5 km/s at the edges of Line 4 (see Figure 2, Line 4, OBS 1) and 4 km/s in the center of the profile. There the P_{c1} is in most cases a secondary arrival, as it is on Line 5, with an apparent velocity of 4.5 km/s (Figure 2, Line 5, OBS 4). A lower crustal refraction (P_{c2}) is then recorded on both lines and is always a first arrival. Starting from here, a general observation is that the first-arrival traveltimes are greatly affected by a rough basement topography (Figures 2 and 3). Very few unambiguous Moho reflections (PmP) are observed (Figure 3, Line 4, OBS 13). Many
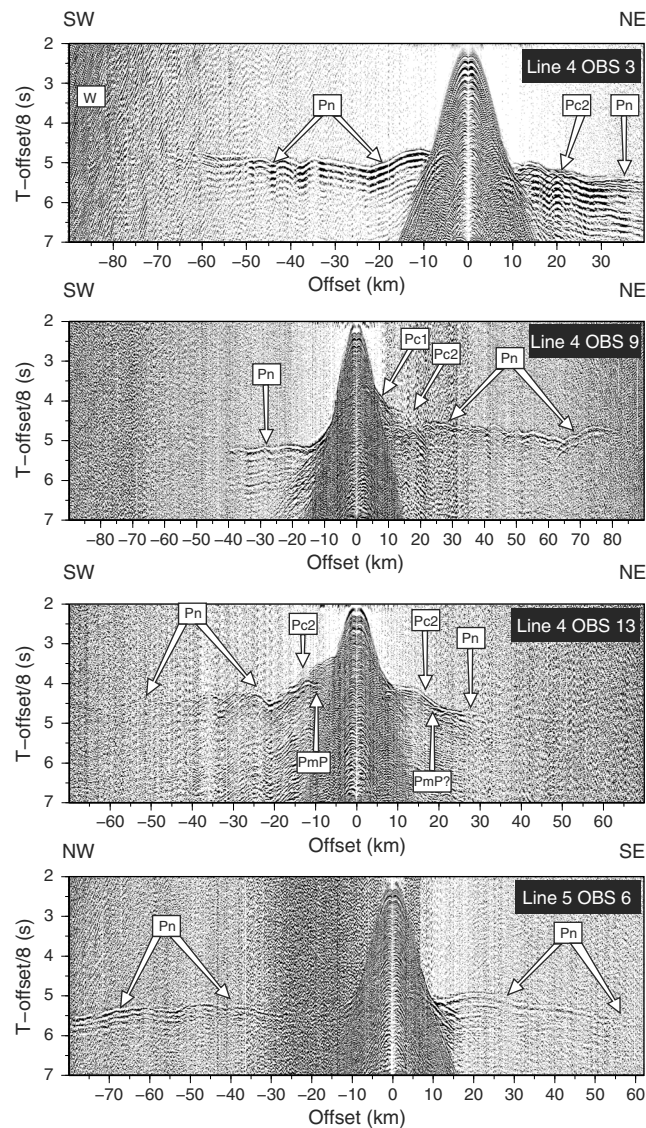
Figure 3. OBS data: mantle arrivals as discussed in the text. The data are band-pass filtered (6–35 Hz) and predictive deconvolution is applied. A reduction velocity of 8.0 km/s is used. OBS13 is the only OBS with a clear PmP arrival. Notice the absence of any crustal arrivals for the negative offsets of Line 4 OBS 3.

OBSs on both lines show a unique high apparent velocity (7 to more than 8 km/s) phase (Pn) from very short offset (10 km) to far offset (Figure 3, Line 5, OBS 6), which indicates a shallow mantle.

2.4. Traveltime Uncertainties

For all phases, the uncertainty of the traveltime picks is related to the signal-to-noise ratio following an empirical relationship [*Zelt and Forsyth*, 1994]. The smallest uncertainty obtained with this method is 20 ms, such as for the water wave and some near-offset arrivals. The lowest signal-to-noise ratio (i.e., when only coherency allows picking) corresponds to a picking uncertainty of 125 ms. This method has the advantage of avoiding bias in the modeling procedure discussed in the next section. Tables 1 and 2 summarize the number of picks per phase and their average uncertainty.

3. Velocity Modeling
3.1. Modeling Strategy

There are two common methods to develop P wave velocity models based on seismic refraction data: forward modeling [*Zelt and Smith*, 1992] and first-arrival traveltime tomography inversion (with or without joint inversion of Moho reflection phases [*Zelt and Barton*, 1998; *Korenaga et al.*, 2000; *Hobro et al.*, 2003; *Van Avendonk et al.*, 2004]). Both methods give non-unique results. Forward modeling potentially leads to overinterpretation as layer geometry and velocity gradients are chosen manually, while traveltime tomography does not suffer as much from overinterpretation. However, in the present case, traveltime tomography is unable to resolve most of the crustal velocities. Indeed, as presented in the previous section, the mantle refraction arrivals represent most of the first-arrival traveltime picks. The crustal first arrivals only have low weight in the inversion, since most of the P_{c1} phase picks are secondary arrivals. Sediment arrivals show the same effect to an even greater degree since they are nearly all secondary arrivals. Thus, the upper 2 km of the velocity depth model cannot be resolved properly in a first-arrival tomography inversion. For this reason, we will primarily use RAYINVR forward modeling [*Zelt and Smith*, 1992] to derive the P wave velocity models. Each observed seismic phase is raytraced using the layer-stripping method (i.e., working from the top of the model downward [*Zelt and Smith*, 1992]). Such an approach is also possible in tomography methods [*Korenaga et al.*, 2000; *Hobro et al.*, 2003; *Van Avendonk et al.*, 2004], as done, e.g., by *Sallarès et al.* [2011, 2013] and *Christeson et al.* [2014].

3.2. Modeling with RAYINVR

The RAYINVR model of Line 4 is composed of nine layers (Figure 5). Below the seafloor, the uppermost three layers correspond to sediments (P_{s1}, P_{s2}, and P_{s3} phases). The next layer is not continuous along the entire model but observed in three deep basins (4A, 4B, and 4C) associated with the P_{s4} phase (Figures 4 and 5). The
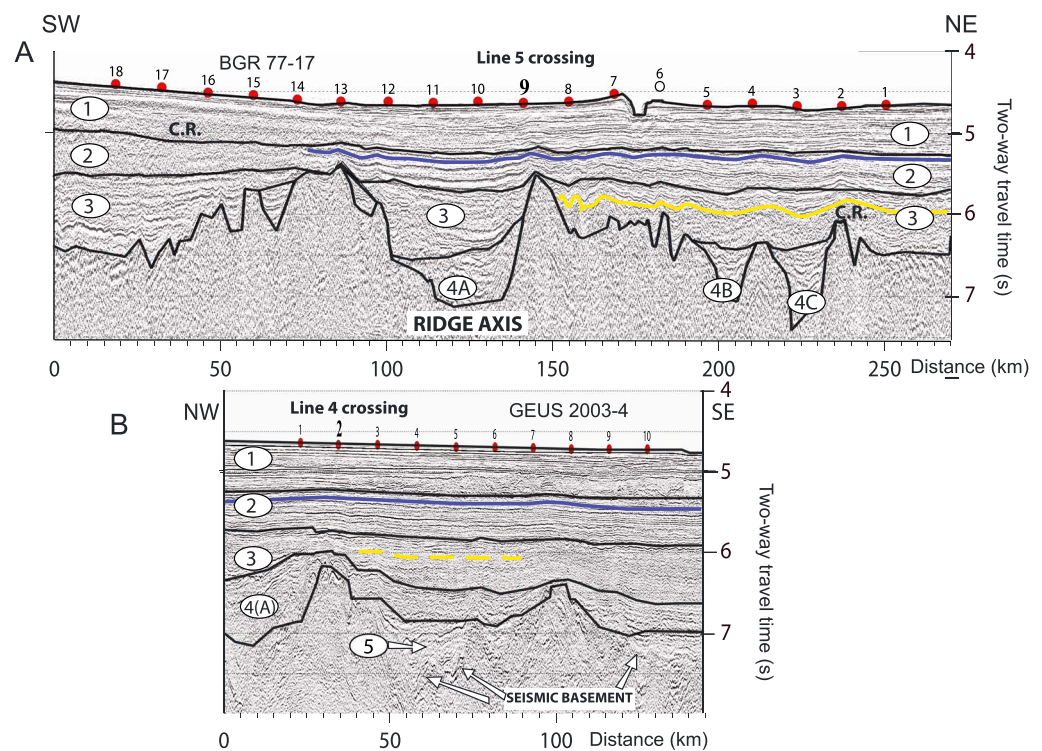
Figure 4. (a) Time migrated section of seismic profile BGR 77-17 [*Chalmers and Laursen*, 1995] across the extinct Labrador Sea spreading axis following SIGNAL Line 4. The blue horizon is dated at 2.5 Ma (R1 in *Arthur et al.* [1989] and *Chalmers and Laursen* [1995]), while the yellow horizon indicates a late Miocene horizon (7.5 Ma, R3/R4 in *Arthur et al.* [1989]). Superimposed are the sedimentary interfaces and seismic basement picked to build the shallow part of the model of Line 4. Layers 1 to 4 are associated with sedimentary phases P_{s1} to P_{s4} as described in the text. (b) Time migrated section of seismic profile GEUS 2003-4 along the extinct Labrador Sea spreading axis and following SIGNAL Line 5. The blue horizon is dated at 2.5 Ma (R1), while the yellow dashed, late Miocene horizon (R3/R4) is estimated from the seismic facies and the sedimentation rates. The base of layer 4 does not always correspond to the seismic basement. Consequently, layer 5 is not a crustal layer, and phase P_{s5} is not a crustal seismic phase. CR: chaotic reflectors.

geometry of the interfaces from the seafloor to the basement is defined by correlation with the coincident reflection seismic Line BGR77-17 (Figure 4). The upper crustal layer is associated with the P_{c1} phase, while the lower crust is associated with the P_{c2} phase. Here we prefer the generic terms "upper crust" and "lower crust" rather than oceanic layer 2 and layer 3, as the slow to ultraslow Labrador Sea spreading ridge may not produce a typical oceanic crust [*Louden et al.*, 1996]. The base of the lower crustal layer is the crust-mantle boundary. In places, the traveltime data require two layers in the mantle, one with a high vertical velocity gradient and the other with a low-velocity gradient extending down to the bottom of the model. Both mantle layers are associated with the Pn phase (Figure 5). The model for Line 5 is also composed of nine layers (Figure 6), similar to Line 4. Sedimentary layers and basement geometries are defined by correlation with the coincident reflection seismic Line GEUS 2003-4 (Figure 4). Tables 1 and 2 summarize the χ^2 and RMS traveltime residuals of each phase. A general display of observed and calculated traveltime is shown in Figures 5 and 6. Record sections of four OBS and details of the modeling are shown in Figures 7 and 8.

3.3. Traveltime Tomography With Tomo2D

To check the robustness of the RAYINVR velocity models, we compare them with results from a first-arrival time tomography using the Tomo2D code [*Korenaga et al.*, 2000]. The forward problem consists of finding the shortest raypath between the shot and the receiver for every ray [*Moser*, 1991]. This is done by combining graph and ray-bending methods [*Moser et al.*, 1992; *Korenaga et al.*, 2000; *Van Avendonk et al.*, 2001]. The inverse problem consists of a reduction of the traveltime residuals between the observed and calculated first-arrival times. The iterative process is done by perturbing velocities using a least squares regularized approach. Because the size of the grid needed for an accurate forward modeling (720×125 nodes for Line 5 and 1350×125 nodes for Line 4, using a node spacing of 200 m) is very large and implies many unknowns (each velocity cell is an unknown), the problem is underconstrained and needs "smoothing" of the velocity perturbations through

Table 1. Seismic Phase, Layer Associated With Refraction Phase, Number of Modeled Rays ($N_{modeled}$), Average Uncertainty of Modeled Rays ($\Delta t_{modeled}$), RMS Residuals Between Observed and Modeled Traveltimes (t_{RMS}), and Normalized χ^2 for All Phases On Signal Line 4

Phase	Associated Layer	$N_{modeled}$	$\Delta t_{modeled}$ (s)	t_{RMS} (s)	χ^2
Direct wave	0	1381	0.021	0.011	0.289
Sediment reflections		2105	0.124	0.040	0.112
P_{s1}	1	428	0.084	0.038	0.782
P_{s2}	2	419	0.034	0.034	1.091
P_{s3}	3	563	0.066	0.032	0.569
P_{s4}	4	221	0.046	0.028	0.837
PbP		963	0.117	0.069	0.353
P_{c1}	5	585	0.053	0.056	2.931
P_{c2}	6	2311	0.084	0.074	2.143
PmP		740	0.094	0.064	0.988
Pn*	7	406	0.099	0.082	1.705
Pn	8	5349	0.119	0.081	0.770
All		15471	0.095	0.065	0.935

"correlation lengths" [*Korenaga et al.*, 2000]. At the top of the crust, and for both lines, we use a horizontal correlation length of 1 km, linearly increasing to 10 km at a depth of 15 km. The vertical correlation length linearly increases from 1 km at the top of the crust to 5 km at a depth of 15 km. The rationale for the increase of correlation length with depth is the prevention of model updates in depth intervals with no turning rays.

In most cases, the Tomo2D code only needs a simple initial velocity model. However, we chose to include the sediment velocities and basement geometry from the RAYINVR model in the initial Tomo2D model. This is necessary because no sedimentary first arrivals are recorded in the data set. Also, the basement topography strongly affects the arrivals and this leads to a very nonlinear problem if the basement is not included in the initial model. Including the RAYINVR sediment velocities is not problematic as the sedimentary layers are flat and the interfaces down to the basement are well constrained by the reflection seismic profiles. Correlation lengths in the sediments are set to 10 km, to prevent model updates in areas where refracted rays do not result in first arrivals. The reference crustal initial model is a linear gradient using a velocity of 4.2 km/s at the basement and 7.7 km/s at 10 km depth, which is the average Moho depth in the RAYINVR models. We then consider that velocities linearly increase to 8.1 km/s at a depth of 14 km. This velocity corresponds to

Table 2. Seismic Phase, Layer Associated With Refraction Phase, Number of Modeled Rays ($N_{modeled}$), Average Uncertainty of Modeled Rays ($\Delta t_{modeled}$), RMS Residuals Between Observed and Modeled Traveltimes (t_{RMS}), and Normalized χ^2 for All Phases on SIGNAL Line 5

| Phase	Associated Layer	$N_{modeled}$	$\Delta t_{modeled}$ (s)	t_{RMS} (s)	χ^2
Direct wave	0	916	0.020	0.008	0.162
Sediment reflections		1191	0.124	0.024	0.037
P_{s1}	1	291	0.096	0.048	0.450
P_{s2}	2	495	0.032	0.015	0.374
P_{s3}	3	955	0.087	0.022	0.071
P_{s4}	4	167	0.069	0.034	0.492
P_{s5}	4,5	288	0.100	0.089	1.584
P*P/PbP		832	0.122	0.098	0.663
P*	5	299	0.056	0.044	2.026
P_{c1}	6	476	0.075	0.058	0.858
PcP/PmP		127	0.098	0.099	1.705
P_{c2}/Pn*	7	1128	0.090	0.057	1.018
Pn	8	3718	0.119	0.085	0.602
All		10883	0.096	0.065	0.576
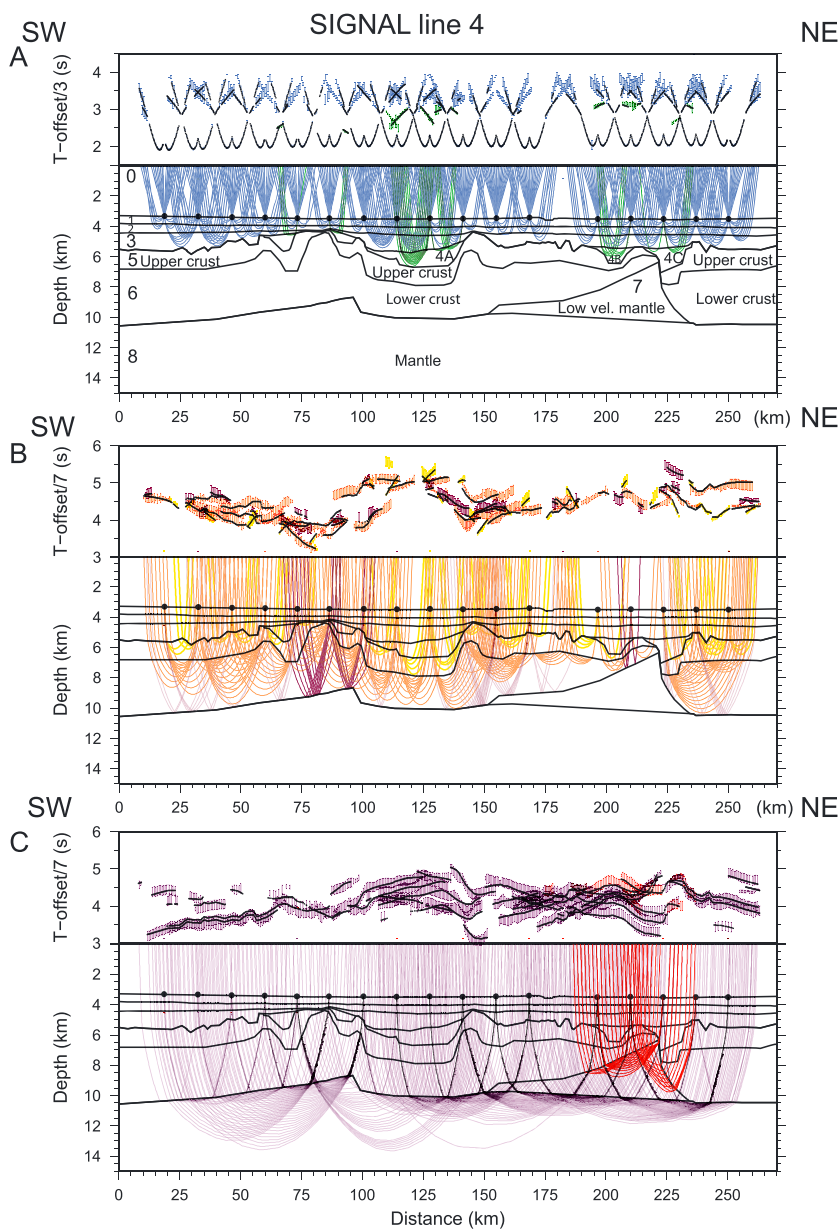
Figure 5. Ray tracing along SIGNAL Line 4. Layers are detailed in the text. (a) The blue rays and traveltime picks are direct water waves and sedimentary phases P_{s1}, P_{s2}, and P_{s3}. The green rays and traveltime picks correspond to phase P_{s4} in the deep, high-velocity basins associated with layer 4. (b) Yellow rays and traveltime picks are related to the P_{c1} phase associated with the upper crustal layer. Orange and purple rays, respectively, correspond to phases P_{c2} (lower crust) and the PmP reflection. (c) Thick red rays turn in layer 7, while purple rays represent the Pn mantle phase. Black lines superimposed on the arrival times and their uncertainties are the calculated traveltimes from the final model (see Figure 9).

mantle rocks that are not affected by serpentinization. The results of a Monte Carlo analysis randomizing this reference initial model will be discussed in section 4.3.2.

4. Results

4.1. SIGNAL Line 4

Figure 9 displays the final RAYINVR model for Line 4. Velocities in the sedimentary layers are 1.75–1.90 km/s for the recent sediments younger than 2.5 Ma (layer S1 and Figure 4), 2.15–2.35 km/s, and 2.35–2.45 km/s, respectively, for layers S2 and S3 (more compacted, late Miocene to Pleistocene sediments, see Figure 4). Layer S4 velocities vary between individual basins. In basin 4A (100–145 km), velocities are 3.5 km/s to 3.8 km/s.
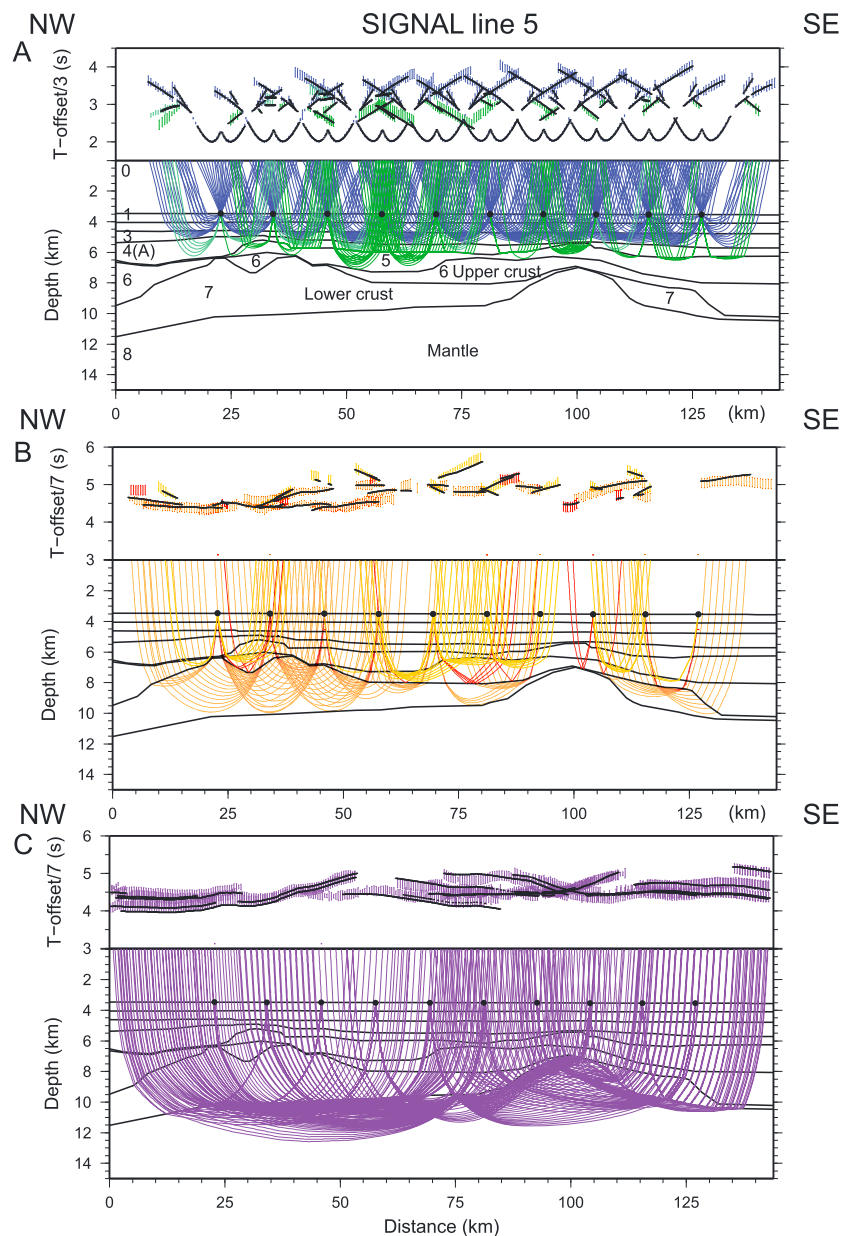
Figure 6. Ray tracing along SIGNAL Line 5. Layer numbers are detailed in the text. (a) The blue rays and traveltime picks are direct water waves and sedimentary phases P_{s1}, P_{s2}, and P_{s3}. The green rays and traveltime picks correspond to phases P_{s4}, P_{s5}, and P* turning in layers 4 and 5 (details in section 4). (b) Yellow rays and traveltime picks are related to the P_{c1} phase associated with the upper crustal layer. Orange and red rays correspond to phases P_{c2} (lower crust) and a crustal reflection, respectively. (c) Purple rays represent the Pn mantle phase. Black lines superimposed on the arrival times and their uncertainties are the calculated traveltimes from the final model (see Figure 9).

In basin 4B (200–210 km), velocities are 3.1 km/s to 3.4 km/s while at 220–230 km (basin 4C), velocities are 3.2 km/s to 3.5 km/s. Both the upper and lower crust display lateral variations in thickness and velocity. We can summarize these variations by describing three distinct crustal domains:

1. The oceanic crust at the edges of the model is composed of a 1.5 km thick upper crustal layer (5.2–5.9 km/s) and a 3.5 km thick lower crustal layer (6.1–7.0 km/s) for a total crustal thickness of 5 km.
2. Between 70 km and 230 km, the velocities of the upper crustal layer are slower (4.0–5.0 km/s). The 1.5 km thick upper crust thins locally in severely faulted areas such as the axial valley slopes and across the 2 km high axial valley walls. The lower crustal layer is characterized by velocities of 6.0–7.0 km/s. The lower crust is thinner than 3.5 km (minimum of 2 km).
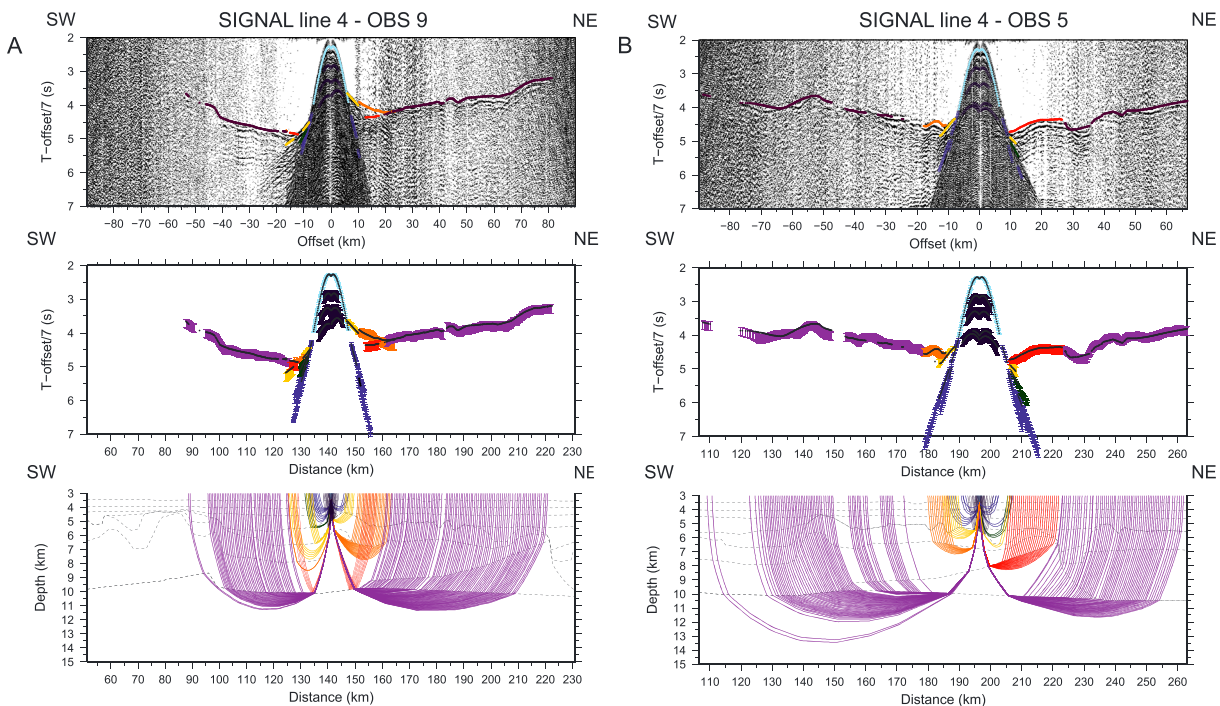
Figure 7. Details of the seismic phases and rays for OBS (right) 5 and (left) 9, Line 4. Calculated arrival times are superimposed on the seismic data. The colors are the same as those described in Figure 5. The data are band-pass filtered (6–35 Hz) and a predictive deconvolution is applied. Traveltimes are displayed with a reduction velocity of 7 km/s.

3. The lower crustal thickness decreases over a 50 km wide section of the profile (180 to 230 km) where velocities between 7.2 and 8.0 km/s are observed. Such velocities are too high to be associated with typical crustal gabbros and are in better agreement with serpentinized mantle [*Minshull et al.*, 1998]. The PxP reflection at OBS 4 (Figure S1) corresponds to the top of this serpentinized mantle, just 1.5 km below the basement. The mantle velocity is 7.7 km/s just below the northeastern axial valley wall (around 70–100 km), where one of the few clear PmP reflections is recorded on OBS 13. A vertical offset of 1 km in the crust-mantle interface is needed to properly model all Pn phases recorded at the southwestern end of the profile.

4.2. SIGNAL Line 5

Figure 9 displays the final RAYINVR model for Line 5. The sedimentary velocities on Line 5 are very similar to those on Line 4. Velocities in the deep basin 4A on Line 5 are 3.2 km/s to 3.8 km/s from 0 to 30 km and 2.9 km/s to 3.1 km/s from 40 to 90 km. A major difference to Line 4 is that the upper crustal layer is not always located immediately below basin 4A. The velocity between the seismic basement and the bottom of basin 4A on Line 5 (Figure 4) is modeled with velocities of 3.8 km/s to 4.3 km/s using P_{s5} and P^* phases. The velocities below the basement are fairly constant in the upper crust and range from 5.0 to 5.3 km/s. Both the geometry of the crust-mantle interface and the lower crustal velocities show significant lateral variations.

Two sections of shallow, high velocities are found in the model:

1. At 20–50 km, the lower crust is 3 km thick and its top is 1 km below the seismic basement. Velocities range from 6.5 km/s at the top to 8 km/s at the bottom, indicating the presence of serpentinized peridotites.
2. Between 90 and 110 km, the lower crust cannot be identified and the mantle velocities of 8.0 km/s are observed 1.5 km below the basement.

Between these two zones (65–85 km), velocities are significantly lower in both the lower crust (6.0 to 7 km/s) and mantle (7.3–8.0 km/s). Several horizontal velocity gradients were tried to define this zone with reduced velocities. The horizontal gradients shown in Figure 9 fit the Pn arrivals best. The zone with reduced velocities can also explain why Pn arrivals from shots located at the southeastern end of the line are not recorded by OBS located at the northwestern end of the line. Similarly, Pn arrivals are not observed on OBS located at the southeastern end of the line for shots fired in the northwest.
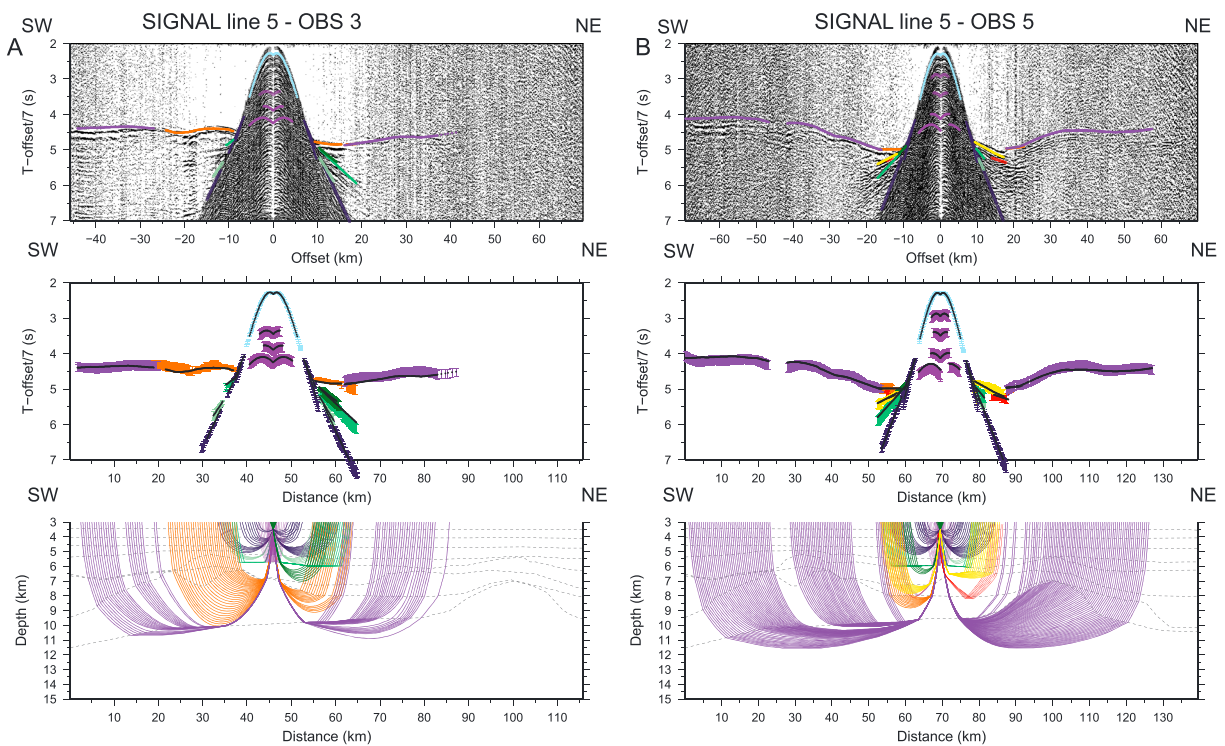
Figure 8. Details of the seismic phases and rays for OBS (right) 4 and (left) 5, Line 5. Calculated arrival times are superimposed on the seismic data. The colors are the same as those described in Figure 6. The data are band-pass filtered (6–35 Hz) and a predictive deconvolution is applied. Traveltimes are displayed with a reduction velocity of 7 km/s.

4.3. Resolution and Robustness of Models

4.3.1. Classic Approach

Tables 1 and 2 give the χ^2 values for each modeled phase. A standard test is to check the compatibility of the RAYINVR models with gravity data. Two-dimensional gravity modeling [*Talwani et al.*, 1959] is performed for both lines. We used generic relationships from *Ludwig et al.* [1970] to convert seismic velocities to densities. The gravity model is compared to satellite-derived free air gravity anomaly (FAA) [*Andersen et al.*, 2010]. The gravity model of Line 4 fits the satellite-derived gravity field very well, with an RMS value of 4.35 mGal. The north-eastern axial valley wall is the worst fit, with a calculated gravity value overestimated by up to 14 mGal. The gravity model of Line 5 is more difficult to determine because of three-dimensional effects since Line 5 is close to the north-eastern axial valley wall. However, the gravity model still fits the satellite FAA reasonably well (7.02 mGal RMS).

Another test of the model reliability is to display the diagonal values of the resolution matrix for the two RAY-INVR models (Figure S2). The resolution matrix calculates the sensitivity of the traveltimes to a perturbation in a velocity node. If modifying a velocity node does not affect the calculated traveltimes, it means that this velocity node is not constrained by the data, corresponding to a resolution value of zero. The more sensitive the traveltime residuals are to a change of a velocity node, the better constrained is that velocity node (with a value closer to 1). A resolution of more than 0.5 is considered to indicate a well-resolved model parameter, whereas values lower than the 0.5 threshold mean that the velocity nodes are not well constrained [*Lutter and Nowack*, 1990]. Overall, Figure S2 indicates good resolution, except at the edges of the models, at layer pinch-outs, and in the areas with lateral velocity variations (e.g., the mantle at the center of Line 5).

However, the resolution matrix is calculated during linearized inversion and gives only the model sensitivity when the final model is almost reached (i.e., for the last iteration) [*Korenaga and Sager*, 2012]. It does not take into account nonlinear sensitivity to the initial model or to variations of the picked traveltimes. Checkerboard tests suffer from the same conceptual problem [*Korenaga and Sager*, 2012], as demonstrated in practice by *Watremez et al.* [2015].
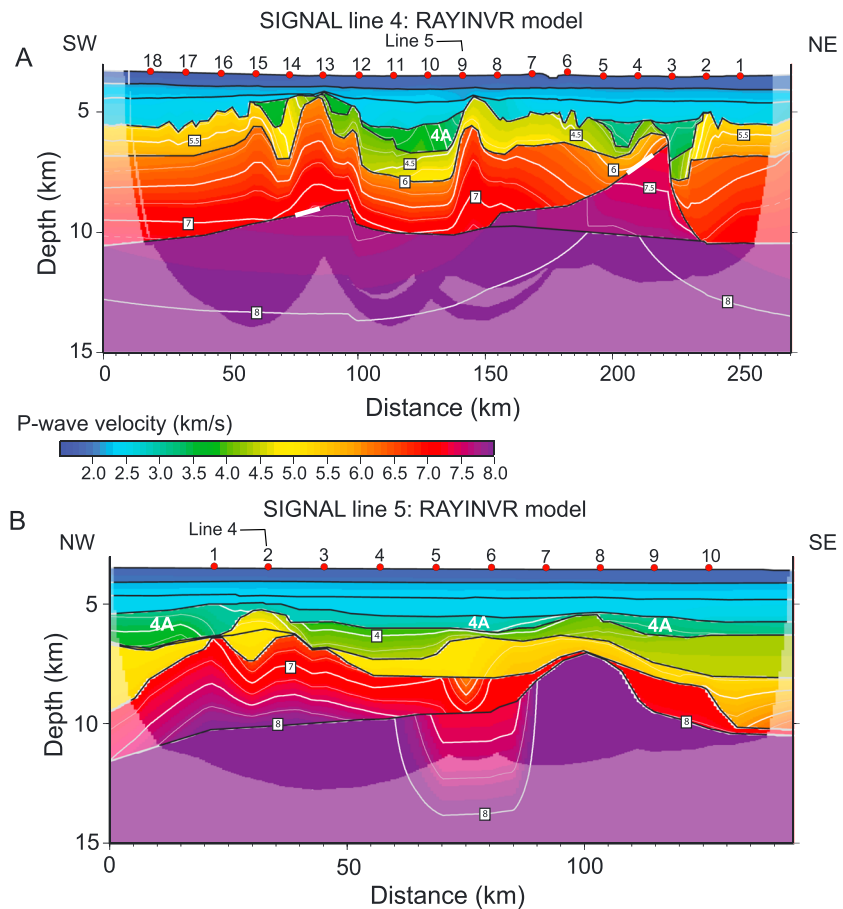
Figure 9. (a) Line 4 RAYINVR final velocity model. Velocity isocontours are superimposed in white (contour interval is 0.25 km/s). A selection of the contours is labeled in km/s. The two thick white segments drawn on the crust-mantle boundary indicate locations where the only two clear PmP reflections originate. (b) Line 5 RAYINVR final velocity field. On both lines, masked areas are not constrained by rays. Red circles show OBS locations.

4.3.2. Monte Carlo Analysis Using Tomo2D

We perform a Monte Carlo analysis using Tomo2D [*Korenaga et al.*, 2000; *Korenaga and Sager*, 2012; *Watremez et al.*, 2015]. The idea is to run many inversions with randomly selected initial models and randomly perturbed traveltime picks. With this independent method, it should be possible to assess which first-order features (shape and depth of the crust-mantle boundary, prominent lateral velocity variations) of the RAYINVR models can be considered well resolved. The three parameters defining the initial crustal velocity model are randomized. The reference 4.2 km/s basement velocity and the 7.7 km/s velocity contour (used as proxy for the base of the crust) can each vary by $\pm 4\%$ (4.0 to 4.4 km/s and 7.4 to 8 km/s, respectively). In addition, the depth of the base of the crust is randomized with a range of ± 1.5 km around the average depth of 10 km. Below the base of the crust, velocities increase linearly to 8.1 km/s at a depth of 14 km. We run 120 inversions for each line so that the statistical average of the parameters are close to the reference parameters. The traveltime picks for each run are also randomly perturbed following the method of *Zhang and Toksöz* [1998].

Figure 10 shows the average Monte Carlo models for both lines. The Monte Carlo standard deviation is displayed in Figure S3 and traveltime residuals are shown in Figure S4. Figure 11 shows the difference ΔV_{MC-i} between the average Monte Carlo model and the average of the initial models. Following *Korenaga and Sager* [2012], we also display $\Delta V_{MC-i} - \sigma$ and $\Delta V_{MC-i} + \sigma$, where σ is the Monte Carlo standard deviation. Structures occurring in all three displays can be considered robust because they do not depend on the initial velocity model. Sharp lateral velocity variations are confirmed, for example, at the southwestern axial valley wall on Line 4 (area E4_2, Figure 11), at 220 km on Line 4 (E4_4), and at 85 km on Line 5 (between E5_3 and E5_4). The low velocity at the center of Line 5 is also confirmed (Area E5_3). One can also notice horizontal structures in ellipses E4_1 and E4_5. These are related to high lower crustal velocity gradients in the initial models.
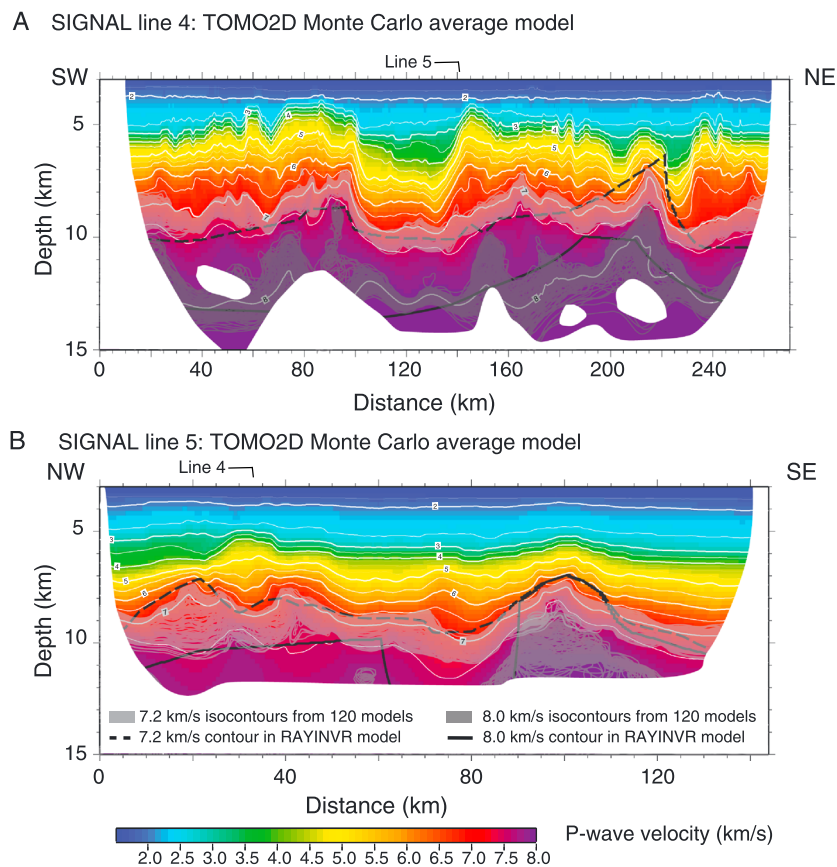
Figure 10. (a) Line 4 Tomo2D Monte Carlo average velocity field. (b) Line 5 Tomo2D Monte Carlo average velocity field. The dashed and the solid black lines show the location of the 7.2 km/s and 8 km/s contours, respectively, in the corresponding RAYINVR models in Figure 9. The shaded areas show the range of the 7.2 km/s and 8.0 km/s contours from the 120 individual Monte Carlo inversions. The velocity model is masked in areas with no ray coverage.

As a result, a common behavior of many inversions is an increase in velocity at the top of the lower crust and in some cases a decrease in velocity at the base of the lower crust. Areas E4_3 and E4_4 show a more homogeneous velocity increase in the crust where the RAYINVR model shows reduced mantle velocities (Line 4, 160–230 km).

4.3.3. Velocities and the Definition of Crustal Thickness

Figure 10 shows that velocity contours typical for the bottom of lower crust (7.2 km/s) and of the mantle (8 km/s) are in good agreement between the RAYINVR and Tomo2D models. An exception to this general good match between the two methods is the northwestern part of Line 5 (0 to 50 km, Figure 10), where the resolution is poor at ~10 km depth (red ellipse, Figure 11). In general, mantle velocities are better constrained on Line 4 (Figures 10 and S5) as a result of longer offset Pn phases. Areas showing mantle or serpentinized mantle velocities (7.2–8.0 km/s) at crustal depths (Line 4, 180–230 km; Line 5, 90–120 km) appear faster in the RAYINVR models. This difference may be due to forward modeling including velocity discontinuities in the crust, contrary to first-arrival tomography.

While the Monte Carlo analysis allows for an estimate on the velocity uncertainties, the few PmP reflections are not sufficient to constrain the uncertainty in the depth of the crust-mantle boundary. In fact, we decided not to use PmP reflections in the Tomo2D inversion since they were too sparse. However, the RAYINVR model features a crust-mantle interface which, when possible, was designed to correspond to the following definition: velocities <7.2 km/s above the interface (gabbros) are separated from (serpentinized) peridotite below. This crust-mantle interface satisfies the observed PmP traveltimes and is continued into zones with no clear PmP observations. If existing, this layer boundary in the velocity model is the best approximation of the Moho. The crustal thickness values given in the discussion are calculated from the basement down to the 7.2 km/s contour, which has an uncertainty of 1 km as indicated in Figure 10.
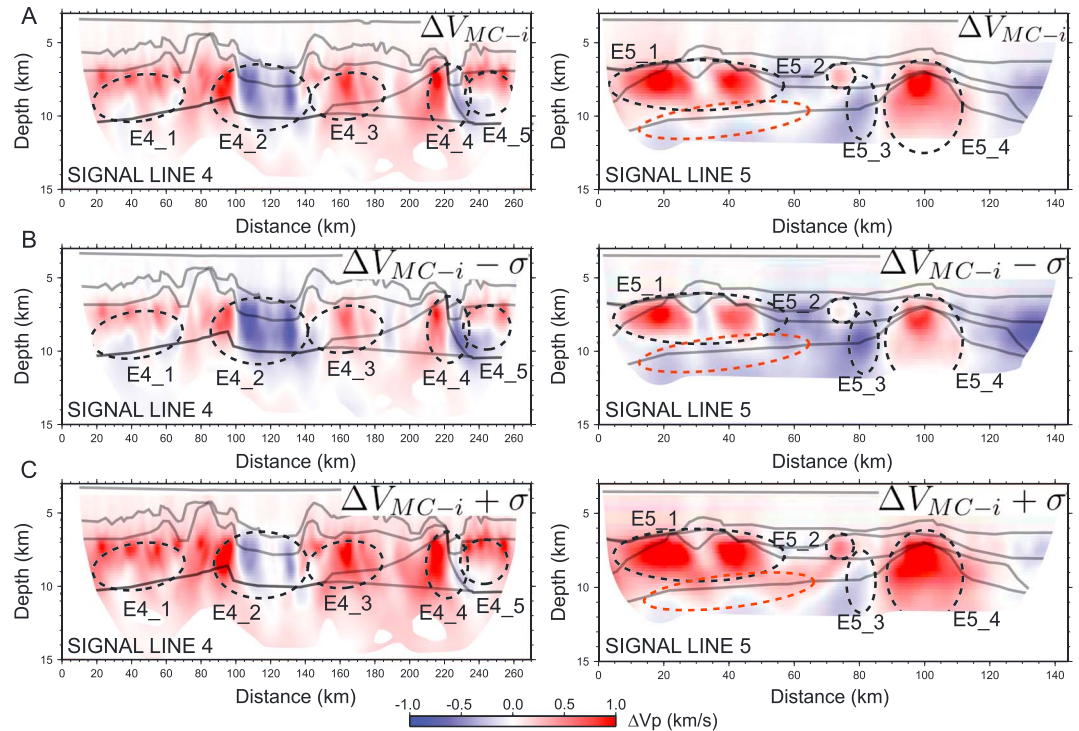
Figure 11. (a) Velocity difference $\Delta V_{\mathrm{MC}-i}$ between the Monte Carlo average model (Figure 10) and the average initial model. (b) $\Delta V_{\mathrm{MC}-i} - \sigma$ with σ as the Monte Carlo standard deviation. (c) $\Delta V_{\mathrm{MC}-i} + \sigma$. The labeled ellipses are discussed in the text and show structures that appear in all three displays (Figures 11a through 11c). The red ellipse shows an area where structures differ in the three displays and where the RAYINVR and Tomo2D velocities do not match (Figure 10). Regions with no ray coverage are shown in white.

5. Discussion
5.1. Variations of Crustal Properties During Oceanic Spreading
5.1.1. Paleocene and Eocene Oceanic Crustal Structures

Previous refraction studies in the Labrador Sea [*Osler and Louden*, 1992, 1995] imaged 3.5 to 5 km thick crust along Line R2 that is parallel to SIGNAL Line 4 at a distance of 100 km to the north-west. On Line 4, with the exception of the segment between 190 km and 240 km (discussed later), our new results are similar to Line R2 but provide considerably more detail (Figure 9). Seismic Lines TLS 90-2 and BGR 77-17 show crustal scale normal faults indicating tectonic extension up to 70% in the area of ultraslow spreading [*Roots and Srivastava*, 1984; *Srivastava and Keen*, 1995]. This extension is believed to occur during the waning stage of the Labrador
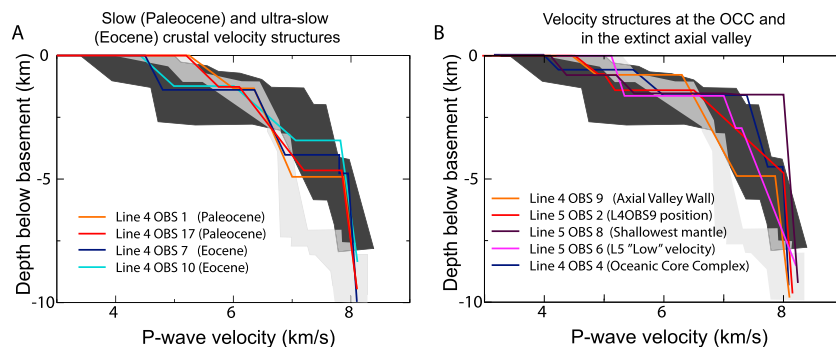
Figure 12. (a) One-dimensional velocities extracted from the velocity models of SIGNAL Line 4 (Figure 9) characterizing Paleocene slow spreading and Eocene ultraslow spreading. Dark-shaded area corresponds to the velocity envelope found in ocean-continent transition zones [*Minshull et al.*, 1998]. Light-shaded area represents the velocity envelope from mature Atlantic-type oceanic crust [*White et al.*, 1992]. (b) Same display with 1-D velocities from SIGNAL Lines 4 and 5 in the extinct axial valley.

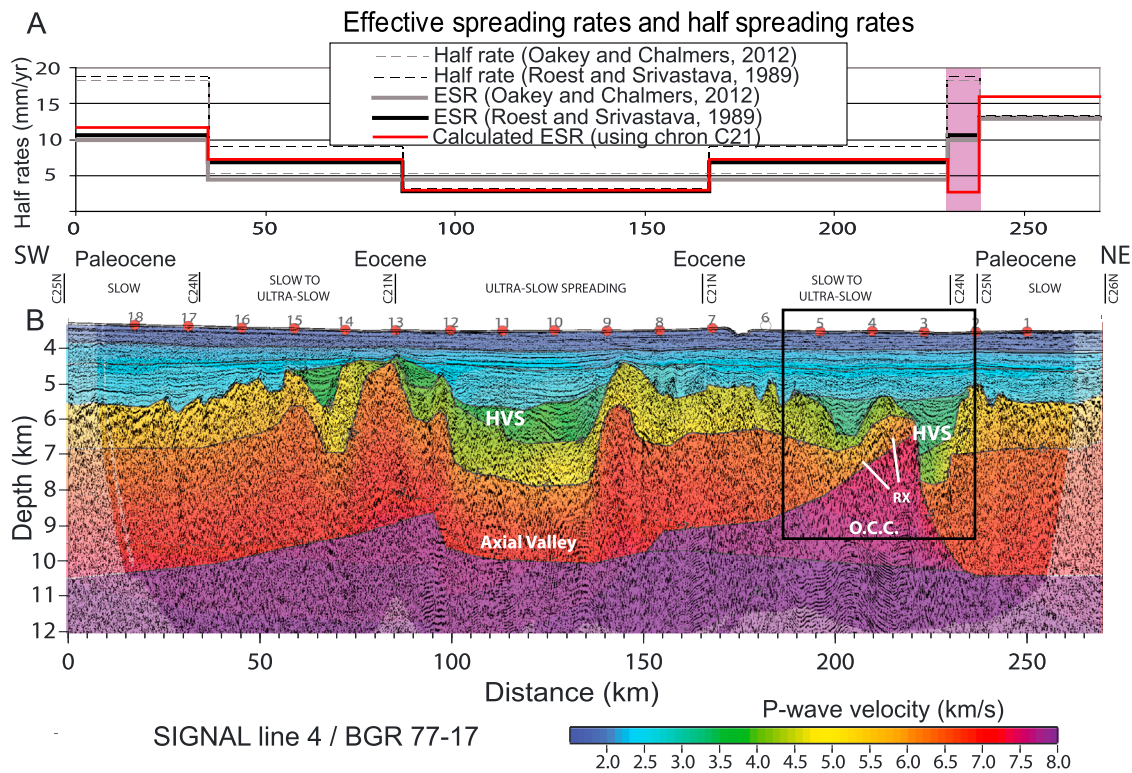**Figure 13.** (a) Half spreading and effective spreading rates (ESR) along SIGNAL Line 4 using stage poles from *Roest and Srivastava* [1989] and *Oakey and Chalmers* [2012]. The "calculated ESR" (red line) is obtained by dividing the ridge perpendicular profile length between two magnetic Chrons by the time span between these Chrons. The purple zone indicates a strong spreading asymmetry (Figure 15). (b) Depth converted BGR 77-17 reflection seismic line using velocities from the Line 4 RAYINVR model. OCC: Oceanic core complex. RX: Reflector from the top of the serpentinized mantle. HVS: High-velocity sediments. The black frame locates Figure S6.

Sea spreading regime in the Eocene, when the magma supply decreased. Associated fractures leading to increased porosity and fluid circulation may explain the lower velocities in the axial valley as observed by *Osler and Louden* [1995] on Line R2. Although the upper crustal velocity cannot be independently checked by the tomography models, SIGNAL Line 4 (Figure 9) clearly confirms low velocities in the upper crust of the axial valley (Figure 12, OBS 7 and 10).

Interestingly, the low velocities in the upper crust are not restricted to the axial valley but also extend across the entire Eocene crust (Chron C24 and younger, Figure 13). By comparison, upper crustal velocities along the Paleocene segments of SIGNAL Line 4 (Chrons C24-C26) are in the upper bound of the velocities of an Atlantic-type oceanic layer 2 [*White et al.*, 1992] (Figure 12). The lateral variations of upper crustal velocities correlate well with changes in the roughness and reflectivity of the basement along the coincident seismic Line BGR 77-17 (Figure 13). Where the seismic basement is faulted and basement reflectivity is weak (Eocene crust), upper crustal velocities are low. Where the basement reflectivity is stronger (Paleocene crust), the upper crustal velocity is closer to normal. The effective half spreading rate is less than 1 cm/yr where the upper crustal velocities are reduced (Figure 13). All these observations strongly support the interpretation of earlier studies [*Roots and Srivastava*, 1984; *Srivastava and Keen*, 1995; *Osler and Louden*, 1992, 1995] that the final stage of spreading in the Labrador Sea was dominated by tectonic extension. The lower crust does not show a clear velocity variation between the Paleocene and Eocene. Instead, the lower crust varies in thickness from 3.5 km during the Paleocene to around 2 km in late Eocene during the waning stage of spreading.

While upper crustal velocities can be explained in relation to variations in basalt porosity (slow for young oceanic crust and faster after hydrothermal circulation) or to tectonic fracturation (in this study), deeper crustal velocities depend more on the lithology. The low-gradient oceanic layer 3, as defined in the Atlantic Ocean (Figure 12) [*White et al.*, 1992], is composed primarily of gabbros. However, Figure 12 shows that even the thickest oceanic crust in the Labrador Sea (Paleocene crust) substantially differs from a mature Atlantic-type oceanic crust. The lower crust in the Labrador Sea is thinner than typical oceanic layer 3, with a slightly
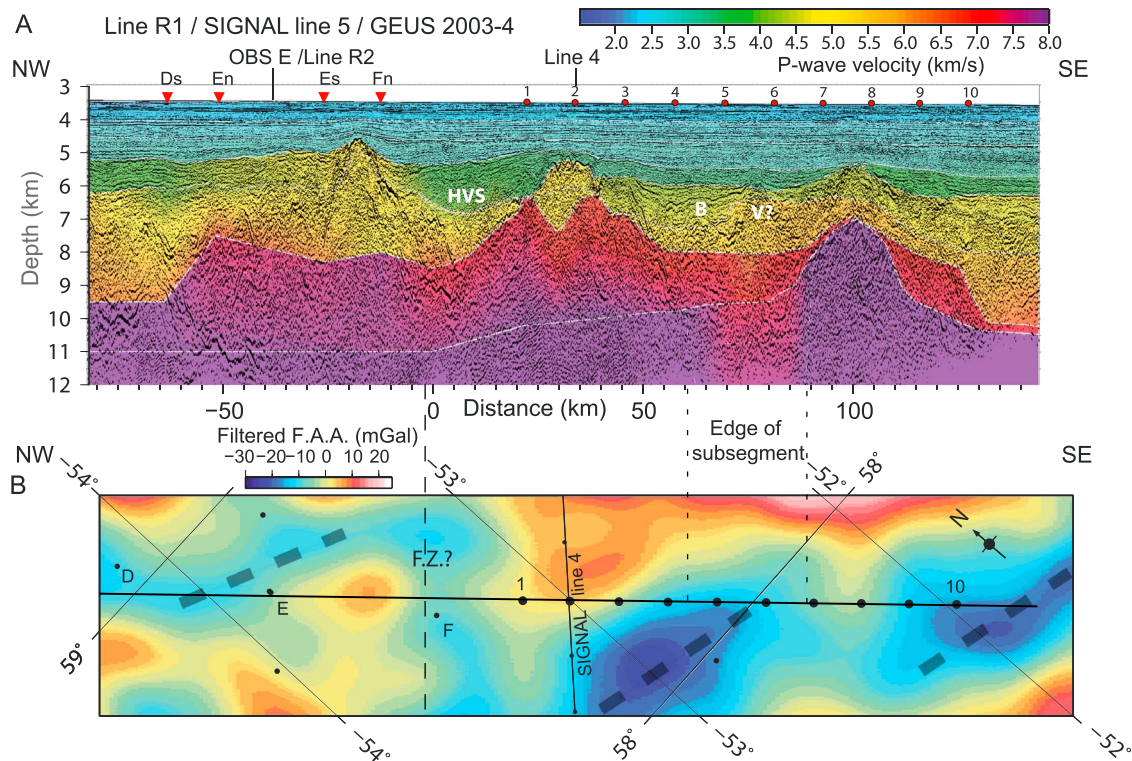
Figure 14. (a) Depth-converted reflection seismic Line GEUS 2003-4 using velocities from the Line 5 RAYINVR model (positive distances) and reconstructed from 1-D velocity profiles from *Osler and Louden* [1992] (negative distances). HVS: High-velocity sediments. B: Possible extrusive basaltic flows, velocities are modeled from phases P$_{55}$ and P*. V: Possible isolated volcano. (b) Filtered satellite free air gravity anomaly oriented along ridge structures oblique to the N-S direction of spreading. Thick dashed lines represent the interpreted last active subsegments of the extinct spreading ridge also shown in Figure 1. The orientation of these subsegments is significantly less oblique to the N-S Greenland-North America plate motion.

higher-velocity gradient. Thin crust produced from magma-poor slow to ultraslow-spreading ridges tend to be composed of serpentinized peridotites intruded by gabbro plutons (the "plum pudding," *Cannat* [1996]). In the Labrador Sea, serpentinization could explain why there are only few clear PmP observations in the data set. The Moho in our models may be more adequately described as a serpentinization front [*Muller et al.*, 1997; *Minshull et al.*, 1998]. As a result, crustal thickness values given in this study may not be used as a proxy for the volume of melt products. Various degrees of serpentinization can also explain the significant lateral variation of the lower crustal thickness and velocities along SIGNAL Line 5 in the axial valley. At the crossing with Line 4, the lower crust has a thickness of 3 km and velocities from 6.5 to 8 km/s (Figure 12). However, around km 100 (Figure 14), the lower crust disappears and is replaced by 8 km/s mantle, which is the velocity of normal, unserpentinized mantle.

5.1.2. A Buried Oceanic Core Complex

The shallow mantle on SIGNAL Line 4 (190–230 km, Figure 13) creates an even thinner crust than the surrounding 3.5 to 5 km thick crust described above. Serpentinized rocks and lower crustal gabbros exhumed at the seafloor are typically dredged on slow-spreading ridges at the inside corners of transform faults [*Dick et al.*, 1981; *Cannat*, 1993; *Tucholke and Lin*, 1994], following the simple view that the center of ridge segments are magma-rich while segment ends tend to be magma-poor [*Buck et al.*, 2005]. The shallow mantle area on SIGNAL Line 4 is located immediately south-west of basin 4C (Figure 4). Just after Chron C25, the deep basin 4C was located in the vicinity of the Cartwright-Julianehaab Fracture Zone (OBS 2 and 3 on Figure 15). However, magnetic anomalies and the free air gravity signature of the shallow mantle structure (beneath OBS 4 in Figure 1) do not show a structural orientation related to the Cartwright-Julianehaab Fracture Zone. A possible explanation is presented in the tectonic evolution shown in Figure 15. After the late Paleocene/early Eocene plate reorganization (post Chron C25), a ridge segment offsets the "cold" Cartwright-Julianehaab fracture zone. As a result, the shallow mantle structure was emplaced relatively far from the fracture zone, at the center of an Eocene spreading ridge segment that is oblique to the N-S oceanic spreading. At that time, oceanic spreading is ultraslow (~1 m/yr full rate) and asymmetric (Figure 13a).
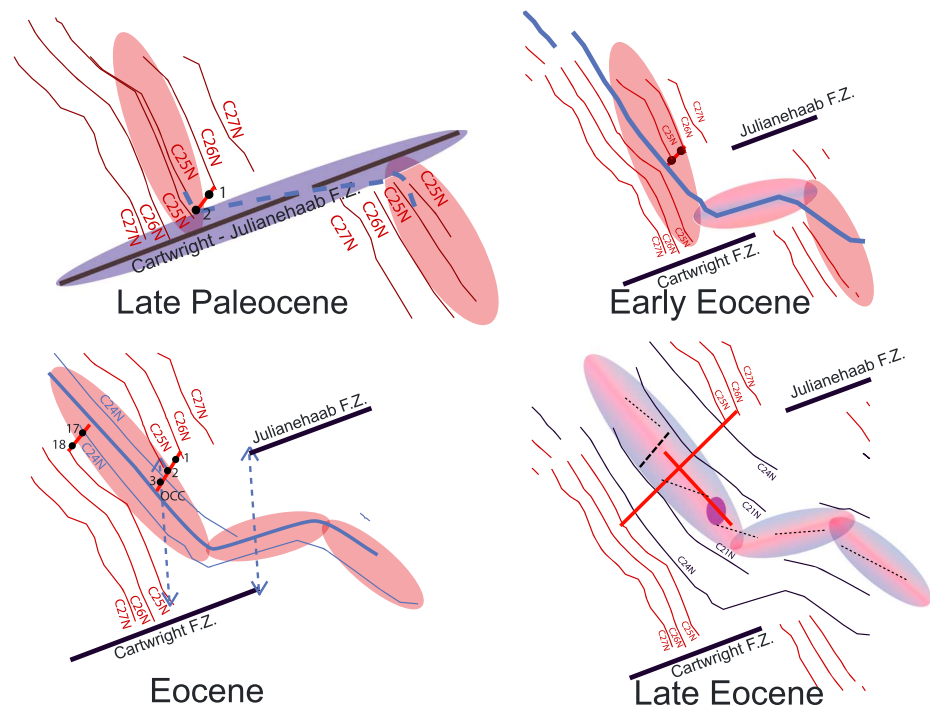
Figure 15. Sketch explaining the evolution of the Labrador Sea spreading ridge system from the Paleocene to late Eocene using magnetic isochrons from *Roest and Srivastava* [1989]. The thick dashed blue line represents the active spreading center cutting through the Cartwright-Julianehaab Fracture Zone (FZ). The dashed blue double arrows represent the new spreading direction after Chron C25. Colored ellipses represent warm (red) and cold (blue) thermal regimes in relation with the geometry of spreading centers and transform faults until the extinction of the Labrador Sea spreading ridges. SIGNAL lines are shown in red with selected OBS positions in black. Thin dashed lines represent interpreted spreading subsegments of the waning stage of spreading from the FAA in Figure 1and the low-velocity zone in Figure 14. The thick dashed line is interpreted as a transform fault, and the purple ellipse is the area of the shallow 8 km/s mantle imaged on Line 5 separating two subsegments.

Slow, asymmetric spreading is a characteristic environment allowing the development of long-lived (1 – 2 Myr) oceanic detachment faults [*Baines et al.*, 2008; *MacLeod et al.*, 2009] unroofing lower crustal and mantle rocks, resulting in the formation of "oceanic core complexes" (OCC). As the fault develops and accommodates extreme extension, the fault dip decreases under the effect of flexural unloading (footwall rollover or rolling hinge model [*Tucholke et al.*, 1998; *Lavier et al.*, 1999]). The exposed low-angle surface of the footwall can be easily recognized in detailed bathymetric maps as a corrugated surface [*Tucholke et al.*, 1998] with a dome shape (Figure S6). Mantle exhumation at mid-ocean ridges was initially thought to be the result of cyclical amagmatic spreading periods [*Karson and Dick*, 1983; *Karson et al.*, 1987]. Today, it is commonly accepted that magmatic accretion is also involved in the process [*Cannat*, 1993; *Escartin et al.*, 2003; *Tucholke et al.*, 2008; *Olive et al.*, 2010]. This can explain the presence of a 1.5 km thick layer with velocities of 4.2 – 6.0 km/s on top of the serpentinized mantle on SIGNAL Line 4, as gabbro bodies are often drilled from these features [*Ildefonse et al.*, 2007]. Reflectors found along Line BGR 77-17 and on the OBS 4 record (RX on Figure S6 and the PxP reflector in Figure 2) may correspond to the interface between serpentinized mantle (>7.2 km/s) and gabbros (6 km/s).

The velocity model of Line 4 requires a direct subvertical contact between the serpentinized mantle body and the sediments in basin 4C. Without such a contact, it is impossible to properly model rays turning toward the fossil-spreading axis for OBS 3, as traveltimes would always be too slow (Figure S7). A very similar pattern is obtained using traveltime tomography (Figure 10). The dimensions of the dome-shaped seismic basement above the serpentinized mantle body and the total length of the detachment up to the breakaway (Figure S6) are very similar to other OCCs at the Mid-Atlantic Ridge or at the SWIR [*Ranero and Reston*, 1999; *Canales et al.*, 2004; *Blackman et al.*, 2009]. However, detachment faults associated with OCCs usually dip toward the ridge axis. Here, it is not the case, and a southward ridge jump must occur after its formation to explain the current situation, with an OCC located to the north of the extinct spreading axis (Figure 15). This southward ridge jump is not documented, and our data are not definitive because SIGNAL Line 4 does not image the conjugate
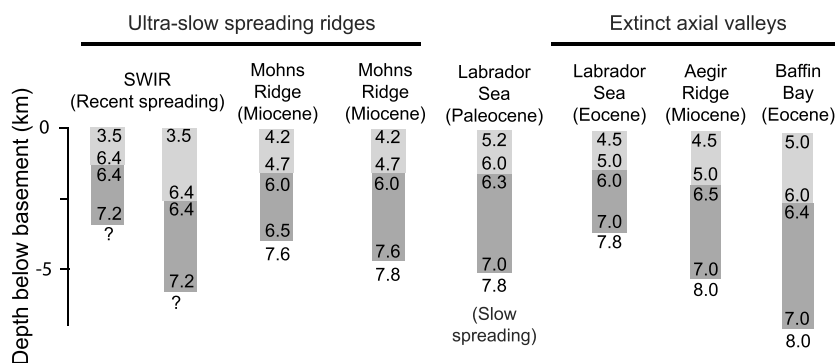
Figure 16. Upper crustal and lower crustal thicknesses and velocities from a selection of ultraslow ridges obtained with velocity modeling methods that are similar to this study. Mohns Ridge velocities (15–17 Ma old crust) are taken from *Klingelhöfer et al.* [2000] and South West Indian Ridge velocities are extrema found away from ridge discontinuities in *Minshull et al.* [2006]. Aegir Ridge velocities are from *Grevemeyer et al.* [1997]. The extinct Baffin Bay axial valley oceanic crustal structure is from *Suckro et al.* [2012]. This velocity structure is close to normal oceanic crust [*White et al.*, 1992].

crust of the OCC area, as illustrated in Figure 15. Hence, basin 4C, between OBS 2 and 4 could indicate an abandoned ridge.

5.1.3. Comparison With Other Ultraslow-Spreading Ridges

In terms of velocity structure and thickness, the Labrador Sea oceanic crust (away from the OCC and ridge discontinuities in the median valley discussed below) is very similar to the oceanic crust at the Mohns Ridge [*Klingelhöfer et al.*, 2000] or the SWIR oceanic crust [*Minshull et al.*, 2006], two well-studied, active ultraslow-spreading ridges (see Figure 16). Half spreading rates are 8 mm/yr and 6 mm/yr for the Mohns Ridge and the SWIR, respectively. These rates are very similar to the Labrador Sea half spreading rate during the Eocene. In the case of the SWIR, the upper crustal layer 2 velocities are slower than the upper crustal velocities in the Labrador Sea, as is expected from young crust in the vicinity of active spreading centers. The topography of the axial valley walls in the Labrador Sea is around 2 km (Figure 9), which is in the middle of the range of observed values compiled by *Dick et al.* [2003].

Three types of seafloor morphology have been observed at the SWIR [*Cannat et al.*, 2006], associated with three spreading regimes [*Buck et al.*, 2005; *Tucholke et al.*, 2008; *Olive et al.*, 2010]:

1. When the melt supply covers more than 50% of the extension rate, oceanic spreading is symmetrical and normal faults with significant offsets are created on both sides of the axis. The resulting seafloor morphology is typical of slow-spreading ridges with significant roughness ("volcanic seafloor" in *Cannat et al.* [2006]);
2. When the melt supply ranges between 30 and 50%, models [*Tucholke et al.*, 2008] show the development of a long-lived detachment fault responsible for OCCs and asymmetric spreading ("corrugated seafloor" in *Cannat et al.* [2006]);
3. If the melt supply is very scarce (less than 30%), the models cannot maintain localization on only one fault and many large-scale normal faults appear on both sides of the ridge axis [*Tucholke et al.*, 2008; *Olive et al.*, 2010] to accommodate the extension ("smooth seafloor" in *Cannat et al.* [2006]).

Most of the oceanic crust in the Labrador Sea imaged by seismic reflection data is typical of slow-spreading ridges and could be classified as a "volcanic seafloor" morphology, particularly the slow-spreading Paleocene crust. The OCC imaged on Line 4 shows that reduced melt supply occurred occasionally during the Labrador Sea spreading history. Regarding the third type of crust observed at the SWIR, the "smooth seafloor," it is difficult to say if it is present in the Labrador Sea, as 3D information on the basement roughness is not available. However, areas of extremely thin crust observed in the extinct median valley certainly corresponds to a very scarce melt supply or to purely tectonic extension.

5.2. Processes During the Waning Stage of Spreading
5.2.1. Cooling of the Asthenosphere and Orientation of the Ridge Segments

Although the structure of the Eocene ultraslow oceanic crust in the Labrador Sea is similar to other present-day active ultraslow-spreading ridges, the tectonic evolution of the crustal structure is sometimes more dramatic, with local exhumation of mantle peridotites (e.g., the OCC). In the axial valley, along SIGNAL Line 5, shallow

mantle indicates a reduced melt supply just before the cessation of spreading. Below, we analyze the along-strike velocity variations by correlation with the free air gravity data.

In the axial valley, Line 5 shows slower, thicker crust (Figure 14, km 70 to 80) where the free air gravity anomaly is negative. This section of the profile is interpreted as the edge of a subsegment of the extinct spreading ridge. Using the free air gravity anomaly map (Figures 1 and 14), several subsegments of the fossil axial valley seem to be less oblique to the plate motion between Greenland and North America when compared to the orientation of magnetic anomalies 21 and 24 and the structures formed at that time (Figure 14). This suggests a last attempt of the spreading ridge segments to rotate in a direction less oblique to the N-S plate motion. Doing so, long first-order ridge segments tend to divide in several subsegments separated by either transform faults (Figure 14, 0 km) or exhumed mantle (Figure 14, 100 km). We suggest that this last attempt to rotate the spreading system into a less oblique orientation is related to thermal factors, based on observations from the SWIR.

At the SWIR, far-field stresses promote diking along segments perpendicular to plate motion during periods with sufficient melt supply [*Dick et al.*, 2003; *Buck et al.*, 2005; *Cannat et al.*, 2008]. During phases with reduced magma supply, the orientation of the ridge segments and ridge flank structures follows the oblique regional ridge direction formed by preexisting shallow asthenospheric temperatures [*Cannat et al.*, 2008]. In the Labrador Sea, this NW-SE direction is inherited from the Paleocene NE-SW spreading direction (red ellipses in Figure 15). This can explain why during the Eocene, free air gravity (Figure 1) and magnetic anomalies show structures remaining oblique to the north-south motion between Greenland and North America. Later, during the waning stage of the Labrador Sea spreading center activity, we infer that the NW-SE regional thermal weakness direction related to the shallow asthenosphere below the ridge system also finally disappeared. As a result, far-field tectonic stresses alone controlled the system. Ridge segments become less oblique as the orientation of the faults becomes more and more perpendicular to the N-S plate motion (Figure 15). This process may also explain the orientation of the ridge segment cutting through the Cartwright-Julianehaab Fracture Zone in late Paleocene/early Eocene. This is the only ridge segment perpendicular to the plate motion in the Labrador Sea, because the asthenosphere along this long fracture zone is not as shallow as under a ridge. An E-W oriented ridge crosses the fracture zone because nothing prevents an orientation of the structures perpendicular to the far field stress.

5.2.2. Comparison With Other Extinct Spreading Centers

While in the Labrador Sea, thin crust and ridge segment rotations are signs that spreading ceased with a low magma supply, this was not the case for all extinct spreading ridges. A recent seismic refraction profile in southern Baffin Bay, north-west of Greenland, imaged oceanic crust that is linked to the Labrador Sea spreading by the transform margin in Davis Strait [*Funck et al.*, 2012; *Suckro et al.*, 2012]. While the axial valley wall topography is similar, the oceanic crustal thickness is very different when compared to the Labrador Sea, although spreading rates are comparable [*Oakey and Chalmers*, 2012]. In southern Baffin Bay, oceanic crustal velocities compare much better with an Atlantic-type oceanic crust, with a normal oceanic layer 3 [*Suckro et al.*, 2012]. The crustal thickness is 6 km at the fossil ridge axis and up to 9 km elsewhere [*Funck et al.*, 2012]. Although a link between crustal thickness and spreading rates can be established from global data sets [*Dick et al.*, 2003], seafloor topography and crustal properties can also vary for a given spreading rate. The temperature of the asthenosphere controls the melt supply [*Purdy et al.*, 1992; *Bown and White*, 1994] and can be independent of other factors like spreading rate. This can explain the variability between Baffin Bay and the Labrador Sea. The southern Baffin Bay oceanic crust lies between volcanic margins and is much closer to the position of the Iceland plume in the Paleocene [*Storey et al.*, 1998]), which is in agreement with a higher asthenospheric temperature and a larger melt supply.

The extinct Aegir Ridge [*Uenzelmann-Neben et al.*, 1992; *Grevemeyer et al.*, 1997] is located in the Norwegian Basin, north of the Faeroe Islands. The Aegir Ridge was active from Chron C24b to Chron C7 [*Talwani and Eldholm*, 1977; *Breivik et al.*, 2006] at slow to ultraslow spreading rates, after which spreading was transferred to the Kolbeinsey Ridge, north of Iceland. Off axis, the oceanic crust formed at the Aegir Ridge shows a typical oceanic crustal thickness (~6 km) [*Grevemeyer et al.*, 1997]. A more recent study with a profile partially overlapping with the line of *Grevemeyer et al.* [1997] shows a much thinner crust (~4 km, [*Breivik et al.*, 2006]) from Chron C21 to the cessation of spreading, in very good agreement with what is observed in the Labrador Sea. However, given the differences between the two studies, caution should be taken when the Aegir Ridge is compared to our study. *Grevemeyer et al.* [1997] did not have seismic reflection data available to define the flat basement in their model. In reality, the basement at the Aegir Ridge is very rough [*Breivik et al.*, 2006],

similar to what is observed on SIGNAL Line 4. Also, the deep basement throughs are filled with basaltic flows [*Uenzelmann-Neben et al.*, 1992] or high-velocity sediments similar to those found on Line GEUS 2003-4 coincident to SIGNAL Line 5 (Figure 14). It seems possible that *Grevemeyer et al.* [1997] included these layers into the oceanic crust (Figure 12) and therefore overestimated the crustal thickness. Even if the absolute crustal thickness in *Grevemeyer et al.* [1997] is overestimated, the relative change in thickness from an off-ridge position to the extinct axis may still be reliable. The crustal thickness moderately decreases by 1 km (down to 5 km) in the fossil axial valley.

Although the three discussed extinct ridges (Labrador Sea, Baffin Bay, and Aegir Ridge) have different crustal thicknesses, the waning stage of accretion seems characterized by a reduced melt supply leading to a decreasing crustal thickness. However, this is not always the case, as episodes of significant volcanism after the abandonment of a spreading ridge have been documented, for instance, in the South China Sea [*Pautot et al.*, 1990] and at the fossil Galapagos Rise [*Haase et al.*, 2011]. Another example is the Shikoku Basin [*Okino et al.*, 1994], where the crust at the extinct spreading axis is sometimes thicker than it is during normal spreading [*Nishizawa et al.*, 2011]. In the Labrador Sea, high velocities associated with phases P_{s5} and P* (4.2 km/s) above the basement on Line 5 (Figure 14) can be related to extrusive volcanism during or after the waning stage of spreading. However, we think that this volcanism is sparse and very moderate. In the Shikoku Basin, large volcanoes at the extinct spreading ridge are associated with thick crust (up to 15 km, [*Nishizawa et al.*, 2011]), which is not the case in the Labrador Sea. The imaged high-velocity sediments (in basins 4A, Figure 13; above the possible extrusive basalts in Figure 14) represent a significant volume and are not restricted to the extinct axial valley (see Figure 13, basins 4B and 4C above the OCC). We infer that most of these sediments originate from gravity currents bringing heavily eroded material from the continental margins. The Oligocene uplift of the SW Greenland continental margin [*Sørensen*, 2006] is a possible source for these high-velocity sediments rather than in situ volcanism. Figure 16 summarizes the crustal structures of the three extinct ridges. Beyond the crustal thickness variations, Figure 16 also shows the reduced upper crustal velocities (4.5 to 5.0 km/s) in the Labrador Sea and on Aegir Ridge, in comparison to velocities of 5.0 to 6.0 km/s in Baffin Bay. The extinct axial valley in Baffin Bay may have experienced much less tectonic extension, in agreement with a larger melt supply.

5.2.3. Tectonic Extension and Spreading

In the fossil axial valley, low upper crustal velocities but also shallow mantle with various degrees of serpentinization provide evidence for significant tectonic extension during and/or after the waning stage of spreading in the Labrador Sea. Hence, it is not a surprise that the crustal velocity structure in the fossil axial valley is in good agreement with velocities of ocean-continent transitional crust (Figure 12) [*Minshull et al.*, 1998, and references therein]. In the case of continental margins, it may take time after rifting to reach a localized nascent spreading and a stable thermal regime that allows a sufficient melt supply, especially as potentially colder continental mantle is exhumed. In the case of the waning stage of spreading at a ridge, the cooling of the asthenosphere and lithosphere might lead to very similar "melt poor" crustal structures and seismic velocities. Faulting imaged on seismic records [*Roots and Srivastava*, 1984; *Srivastava and Keen*, 1995] (Figure 4) also favor significant tectonic extension in the Labrador Sea. Tectonic extension, however, can be associated with oceanic spreading with low melt supply (as discussed above), or to pure tectonism after emplacement of the crust. In the first case, faulting is localized at the ridge axis, while in the second case, extensional faulting can continue for a while away from the ridge [*Srivastava and Keen*, 1995]. In the Labrador Sea, several observations tend to favor such "thinning" of the crust, without necessarily excluding tectonic extension during spreading. First, both Tomo2D and RAYINVR models (Figures 10 and 13) show a sudden step in the velocity isocontours at the southwestern axial valley wall, as well as an extreme thinning of the upper crust at the same location in the RAYINVR model (Figure 13). *Srivastava and Keen* [1995] image several fault reflectors deep in the lower crust at the axis walls, implying an entirely brittle crust. Such faults are ideal to explain the sharp lateral velocity variations at the southwestern axial valley wall in our models. A last observation suggests faulting in a brittle crust, away from spreading: the seismic images of the oceanic crust in the vicinity of the extinct spreading center along MCS Line AGC 90-2 [*Srivastava and Keen*, 1995] near to Line R2 [*Louden et al.*, 1996] are similar to the most seaward hyperextended continental crust observed at the Nova Scotia continent-ocean transition zone. *Wu et al.* [2006] observe in both cases very distinct tilted blocks of ~10 km width. This suggests a similar brittle thickness, different from what it would be during active spreading. This further suggests that if spreading is initially slow after continental rifting, normal faults and tilted blocks are not a good marker of the continent-ocean boundary [*Srivastava and Keen*, 1995]. Nascent oceanic spreading in ocean-continent transition zones can sometimes also be characterized by a smoother basement that compares better to the

"smooth seafloor" category [*Minshull*, 2009]. In the Labrador Sea, there is no evidence for such a regime prior to cessation of spreading, or it is too short to be detected.

6. Conclusions

The SIGNAL 2009 cruise acquired two seismic refraction profiles along and across the now extinct Labrador Sea spreading ridge. The oceanic crustal thickness is thinner than typical oceanic crust. The Paleocene crust is up to 5 km thick and formed at slow spreading rates. In contrast, the Eocene crust is 3.5 km thick and formed by ultraslow spreading. In some areas of the extinct axial valley, the oceanic crust is almost absent and mantle rocks are found close to the basement. The waning stage of accretion is characterized by a fractured basement with weak reflections and upper crustal velocities of 4.5 km/s. These velocities compare to 5.2 km/s farther away from the extinct spreading axis, where spreading was slow. The new results confirm previous interpretations [*Osler and Louden*, 1992, 1995; *Srivastava and Keen*, 1995] of a waning stage of spreading that is dominated by tectonic extension, with faulting and fluid circulation leading to varying degrees of serpeninization of the mantle.

The velocity structure of the oceanic crust in the Labrador Sea does not represent a typical, mature Atlantic type oceanic crust. Along most of the across-axis SIGNAL Line 4, the oceanic crustal velocity structure is similar to results from some other studies of active or extinct ultraslow-spreading ridges (SWIR, Mohns Ridge, late Aegir Ridge), but differs from the much thicker Baffin Bay oceanic crust and some thicker segments of the SWIR [*Niu et al.*, 2015]. This suggests that thermal regimes, in addition to spreading rates, control the oceanic spreading style [*Niu et al.*, 2015]. Away from the axial valley, the crustal velocity structure common to "melt-limited" slow to ultraslow ridges is characterized by (1) a 1.5–2 km thick upper crust with velocities ranging from 4.0 km/s to 6.0 km/s, depending on the degree of fracturing and the age of the crust, (2) a 2 to 3.5 km thick lower crust with velocities between 6 km/s and 7.5 km/s. This velocity structure corresponds neither to typical oceanic crust nor to the transitional crust found at passive margins. In terms of lithologies, this kind of velocity structure is compatible with a mix of serpentinites and gabbro plutons as in the "plum pudding" model [*Cannat*, 1996].

In some areas of the Labrador Sea, the velocity structure differs even further from a typical oceanic crust. This is the case for an interpreted Oceanic Core Complex formed just after plate reorganization in the early Eocene, as a new spreading segment cuts through the "cold" Cartwright-Julianehaab Fracture Zone. Mantle rock with velocities of 8 km/s is found at shallow depth beneath the extinct axial valley just 1.5 km below the basement. The velocity structure in these areas of very thin crust is similar to continent-ocean transition zones. Both the velocity models and the faults imaged on published seismic reflection profiles suggest that the crust is almost entirely brittle when tectonic extension occurs. In this regard, the waning stage of oceanic spreading may not be different from the Eocene ultraslow spreading, but the preexisting faults in the oceanic crust around the fossil axial valley may remain active in a colder thermal regime. Since Line 5 only samples one of the highly tectonized axial valley walls, more details on the structure at the center of the fossil axial valley could help us to better constrain the chronology of the "extinction" processes (e.g., tectonic extension, cessation of spreading, and residual extrusive volcanism).

References

Andersen, O., P. Knudsen, and P. Berry (2010), The DNSC08GRA global marine gravity field from double retracked satellite altimetry, *J. Geod.*, *84*(3), 191–199, doi:10.1007/s00190-009-0355-9.

Arthur, M. A., S. Srivastava, M. Kaminski, R. Jarrard, and J. Osler (1989), Seismic stratigraphy and history of deep circulation and sediment drift development in Baffin Bay and the Labrador Sea, *Proc. Ocean Drill. Program Sci. Results*, *105*, 957–988.

Baines, A. G., M. J. Cheadle, B. E. John, and J. J. Schwartz (2008), The rate of oceanic detachment faulting at Atlantis Bank, SW Indian Ridge, *Earth Planet. Sci. Lett.*, *273*, 105–114, doi:10.1016/j.epsl.2008.06.013.

Blackman, D., J. Canales, and A. Harding (2009), Geophysical signatures of oceanic core complexes, *Geophys. J. Int.*, *178*, 593–613, doi:10.1111/j.1365-246X.2009.04184.x.

Bouysse, P., et al. (2010), Geological map of the world, 3rd ed., Commission for the Geological Map of the World (CGMW-UNESCO). [Available at http://ccgm.org/en/maps/93-carte-geologique-du-monde-a-125-000-000-9782917310045.html.]

Bown, J. W., and R. S. White (1994), Variation with spreading rate of oceanic crustal thickness and geochemistry, *Earth Planet. Sci. Lett.*, *121*(3–4), 435–449.

Breivik, A. J., R. Mjelde, J. I. Faleide, and Y. Murai (2006), Rates of continental breakup magmatism and seafloor spreading in the Norway Basin-Iceland plume interaction, *J. Geophys. Res.*, *111*, B07102, doi:10.1029/2005JB004004.

Buck, W. R., L. L. Lavier, and A. N. B. Poliakov (2005), Modes of faulting at mid-ocean ridges, *Nature*, *434*, 719–723, doi:10.1038/nature03358.

Canales, J. P., B. E. Tucholke, and J. A. Collins (2004), Seismic reflection imaging of an oceanic detachment fault: Atlantic megamullion (Mid-Atlantic Ridge, 30°10′N), *Earth and Planet. Sci. Lett.*, *222*, 543–560, doi:10.1016/j.epsl.2004.02.023.

Cannat, M. (1993), Emplacement of mantle rocks in the seafloor at mid-ocean ridges, *J. Geophys. Res.*, *98*, 4163–4172.

Cannat, M. (1996), How thick is the magmatic crust at slow spreading oceanic ridges, *J. Geophys. Res.*, *101*, 2847–2857.

Cannat, M., D. Sauter, V. Mendel, E. Ruellan, K. Okino, J. Escartin, V. Combier, and M. Baala (2006), Modes of seafloor generation at a melt-poor ultraslow-spreading ridge, *Geology*, *34*(7), 605–608, doi:10.1130/G22486.1.

Cannat, M., D. Sauter, A. Bezos, C. Meyzen, E. Humler, and M. Le Rigoleur (2008), Spreading rate, spreading obliquity, and melt supply at the ultraslow spreading Southwest Indian Ridge, *Geochem. Geophys. Geosyst.*, *9*, Q04002, doi:10.1029/2007GC001676.

Chalmers, J. A., and K. H. Laursen (1995), Labrador Sea—The extent of continental and oceanic-crust and the timing of the onset of sea-floor spreading, *Mar. Pet. Geol.*, *12*(2), 205–217, doi:10.1016/0264-8172(95)92840-S.

Chian, D., and K. Louden (1994), The continent-ocean crustal transition across the southwest Greenland margin, *J. Geophys. Res.*, *99*(B5), 9117–9135.

Chian, D., and K. E. Louden (1995), Crustal structure of the Labrador Sea conjugate margin and implications for the formation of nonvolcanic continental margins, *J. Geophys. Res.*, *100*, 24,239–24,253.

Christeson, G. L., H. J. A. Van Avendonk, I. O. Norton, J. W. Snedden, D. R. Eddy, G. D. Karner, and C. A. Johnson (2014), Deep crsutal structure in the eastern Gulf of Mexico, *J. Geophys. Res. Solid Earth*, *119*, 6782–6801, doi:10.1002/2014JB011045.

Dick, H. J. B., G. A. Thompson, and W. B. Bryan (1981), Low angle faulting and steady-state emplacement of plutonic rocks at ridge-transform intersections, *Eos Trans. AGU*, *62*, 406.

Dick, H. J. B., J. Lin, and H. Schouten (2003), An ultraslow-spreading class of oceanic ridge, *Nature*, *426*, 405–412, doi:10.1038/nature02128.

Ehlers, B. M., and W. Jokat (2009), Subsidence and crustal roughness of ultra-slow spreading ridges in the North Atlantic and the Arctic Ocean, *Geophys. J. Int.*, *177*, 451–462, doi:10.1111/j.1365-246X.2009.04078.x.

Escartin, J., C. Mével, C. J. MacLeod, and A. M. McCaig (2003), Constraints on deformation conditions and the origin of oceanic detachments: The Mid-Atlantic Ridge core complex at 15°45'N, *Geochem. Geophys. Geosyst.*, *4*(8), 1067, doi:10.1029/2002GC000472.

Funck, T., J. R. Hopper, H. C. Larsen, K. E. Louden, B. E. Tucholke, and W. S. Holbrook (2003), Crustal structure of the ocean-continent transition at Flemish Cap: Seismic refraction results, *J. Geophys. Res.*, *108*(B11), 2531, doi:10.1029/2003JB002434.

Funck, T., H. R. Jackson, K. E. Louden, and F. Klingelhöfer (2007), Seismic study of the transform-rifted margin in Davis Strait between Baffin Island (Canada) and Greenland: What happens when a plume meets a transform, *J. Geophys. Res.*, *112*, B04402, doi:10.1029/2006JB004308.

Funck, T., S. A. Dehler, C. B. Chapman, M. Delescluse, J. Iuliucci, R. Iuliucci, W. Judge, P. Meslin, and M. Ruhnau (2009), Cruise report of the SIGNAL 2009 refraction seismic cruise (Hudson 2009-019): Joint Danish-Canadian UNCLOS expedition to the Eirik Ridge, to the extinct Labrador Sea spreading axis and to Orphan Basin off Newfoundland, Rep. Geol. Surv. of Denmark and Greenland 2009/74, Geol. Surv. of Denmark and Greenland, p. 114, Copenhagen, Denmark.

Funck, T., K. Gohl, V. Damm, and I. Heyde (2012), Tectonic evolution of southern Baffin Bay and Davis Strait: Results from a seismic refraction transect between Canada and Greenland, *J. Geophys. Res.*, *117*, B04107, doi:10.1029/2011JB009110.

Grevemeyer, I., W. Weigel, R. B. Whitmarsh, F. Avedik, and G. A. Dehghani (1997), The aegir rift: Crustal structure of an extinct spreading axis, *Mar. Geophys. Res.*, *19*(1), 1–23.

Haase, K. M., M. Regelous, R. A. Duncan, P. A. Brandl, N. Stroncik, and I. Grevemeyer (2011), Insight into mantle composition and mantle melting beneath mid-ocean ridges from postspreading volcanism on the fossil Galapagos Rise, *Geochem. Geophys. Geosyst.*, *12*, QOAC11, doi:10.1029/2010GC003482.

Hinz, K., H.-U. Schluter, A. Grant, S. Srivastava, D. Umpleby, and J. Woodside (1979), Geophysical transects of the Labrador Sea: Labrador to southwest Greenland, *Tectonophysics*, *59*, 151–183.

Hobro, J. W. D., S. Singh, and T. Minshull (2003), Three-dimensional tomographic inversion of combined reflection and refraction seismic traveltime data, *Geophys. J. Int.*, *152*, 79–93, doi:10.1046/j.1365-246X.2003.01822.x.

Ildefonse, B., D. Blackman, B. E. John, Y. Ohara, D. J. Miller, and C. J. MacLeod (2007), Oceanic core complexes and crustal accretion at slow-spreading ridge, *Geology*, *35*(7), 623–626, doi:10.1130/G23531A.1.

Jokat, W., and M. C. Schmidt-Aursch (2007), Geophysical characteristics of the ultraslow spreading Gakkel Ridge, Arctic Ocean, *Geophys. J. Int.*, *168*, 983–998, doi:10.1111/j.1365-246X.2006.03278.x.

Jokat, W., O. Ritzmann, M. Schmidt-Aursch, S. Drachev, S. Gauger, and J. Snow (2003), Geophysical evidence for reduced melt production on the Arctic ultraslow Gakkel mid-ocean ridge, *Nature*, *423*, 962–965, doi:10.1038/nature01706.

Karson, J. A., and H. J. B. Dick (1983), Tectonics of ridge-transform intersections at the Kane Fracture Zone, *Mar. Geophys. Res.*, *6*, 51–98.

Karson, J. A., et al. (1987), Along-axis variations in seafloor spreading in the MARK area, *Nature*, *328*, 681–685.

Keen, C. E., K. Dickie, and S. A. Dehler (2012), The volcanic margins of the northern Labrador Sea: Insights to the rifting process, *Tectonics*, *31*, TC1011, doi:10.1029/2011TC002985.

Klingelhöfer, F., L. Géli, L. Matias, N. Steinsland, and J. Mohr (2000), Crustal structure of a super-slow spreading centre: A seismic refraction study of Mohns Ridge, 72°N, *Geophys. J. Int.*, *141*, 509–526, doi:10.1046/j.1365-246x.2000.00098.x.

Korenaga, J., and W. W. Sager (2012), Seismic tomography of Shatsky Rise by adaptative importance sampling, *J. Geophys. Res.*, *117*, B08102, doi:10.1029/2012JB009248.

Korenaga, J., W. S. Holbrook, G. M. Kent, P. B. Kelemen, R. S. Detrick, H. C. Larsen, J. R. Hopper, and T. Dahl-Jensen (2000), Crustal structure of the Southeast Greenland margin from joint refraction and reflection seismic tomography, *J. Geophys. Res.*, *105*, 21,591–21,614, doi:10.1029/2000JB900188.

Lavier, L. L., W. R. Buck, and A. N. B. Poliakov (1999), Self-consistent rolling-hinge model for the evolution of large-offset low-angle normal faults, *Geology*, *27*, 1127–1130.

Lawver, L. A., and R. D. Müller (1994), Iceland hotspot track, *Geology*, *22*, 311–314.

Louden, K. E., J. C. Osler, S. P. Srivastava, and C. E. Keen (1996), Formation of oceanic crust at slow spreading rates: New constraints from an extinct spreading center in the Labrador Sea, *Geology*, *24*(9), 771–774.

Ludwig, W., J. Nafe, and C. Drake (1970), Seismic refraction, in *The Sea*, vol. 4, edited by A. E. Maxwell, pp. 53–84, Wiley-Interscience, New York.

Lundin, E., and A. G. Doré (2002), Mid-cenozoic post-breakup deformation in the 'passive' margins bordering the Norwegian-Greenland Sea, *Mar. Pet. Geol.*, *19*, 79–93, doi:10.1016/S0264-8172(01)00046-0.

Lutter, W., and R. Nowack (1990), Inversion for crustal structure using reflections from the PASSCAL Ouachita experiment, *J. Geophys. Res.*, *95*, 4633–4646.

MacLeod, C. J., R. C. Searle, B. J. Murton, J. F. Casey, C. Mallows, S. C. Unsworth, K. L. Achenbach, and M. Harris (2009), Life cycle of oceanic core complexes, *Earth Planet. Sci. Lett.*, *287*, 333–334, doi:10.1016/j.epsl.2009.08.016.

McKenzie, D., and J. G. Sclater (1971), The evolution of the Indian Ocean since the late Cretaceous, *Geophys. J. R. Astron. Soc.*, *25*, 437–528.

Michael, P. J., et al. (2003), Magmatic and amagmatic seafloor generation at the ultraslow-spreading Gakkel Ridge, Arctic Ocean, *Nature*, *423*, 956–961, doi:10.1038/nature01704.

Minshull, T. A. (2009), Geophysical characterisation of the ocean-continent transition at magma-poor rifted margins, *C. R. Geosci.*, *341*(5), 382–393, doi:10.1016/j.crte.2008.09.003.

Minshull, T. A., M. R. Muller, C. J. Robinson, R. S. White, and M. J. Bickle (1998), Is the oceanic Moho a serpentinization front?, in *Modern Ocean Floor Processes and the Geological Record*, edited by R. A. Mills and K. Harrison, *Geol. Soc. Spec. Publ.*, London, *148*, 71–80.

Minshull, T. A., M. R. Muller, and R. S. White (2006), Crustal structure of the Southwest Indian Ridge at 66°E: Seismic constraints, *Geophys. J. Int.*, *166*, 1–11, doi:10.1111/j.1365-246X.2006.03001.x.

Moser, T. (1991), Shortespath calculation of seismic rays, *Geophysics*, *56*, 59–67.

Moser, T., G. Nolet, and R. Snieder (1992), Ray bending revisited, *Bull. Seismol. Soc. Am.*, *82*, 259–288.

Muller, M. R., C. J. Robinson, T. A. Minshull, R. S. White, and M. J. Bickle (1997), Thin crust beneath ocean drilling program borehole 735B at the Southwest Indian Ridge?, *Earth Planet. Sci. Lett.*, *148*, 93–107.

Nishizawa, A., K. Kaneda, and M. Oikawa (2011), Backarc basin oceanic crust and uppermost mantle seismic velocity structure of the Shikoku Basin, south of Japan, *Earth Planets Space*, *63*, 151–155, doi:10.5047/eps.2010.12.003.

Niu, X., A. Ruan, J. Li, T. Minshull, D. Sauter, Z. Wu, X. Qiu, M. Zhao, Y. J. Chen, and S. Singh (2015), Along-axis variation in crustal thickness at the ultraslow spreading Southwest Indian Ridge (50°E) from a wide-angle seismic experiment, *Geochem. Geophys. Geosyst.*, *16*, 468–485, doi:10.1002/2014GC005645.

Oakey, G. N., and J. A. Chalmers (2012), A new model for the Paleogene motion of Greenland relative to North America: Plate reconstructions of the Davis Strait and Nares Strait regions between Canada and Greenland, *J. Geophys. Res.*, *117*, B10401, doi:10.1029/2011JB008942.

Okino, K., Y. Shimakawa, and S. Nagaoka (1994), Evolution of the Shikoku Basin, *J. Geomagn. Geoelec.*, *46*, 463–479.

Olive, J.-A., M. D. Behn, and B. E. Tucholke (2010), The structure of oceanic core complexes controlled by the depth distribution of magma emplacement, *Nat. Geosci.*, *491*–495(3), doi:10.1038/NGEO888.

Osler, J. C., and K. E. Louden (1992), Crustal structure of an extinct rift axis in the Labrador Sea: Preliminary results from a seismic refraction survey, *Earth Planet. Sci. Lett.*, *108*(4), 243–258.

Osler, J. C., and K. E. Louden (1995), Extinct spreading center in the Labrador Sea: Crustal structure from a two-dimensional seismic-refraction velocity model, *J. Geophys. Res.*, *100*(B2), 2261–2278.

Patriat, P., D. Sauter, M. Munschy, and L. Parson (1997), A survey of the Southwest Indian Ridge axis between Atlantis II fracture zone and the Indian Ocean triple junction: Regional setting and large scale segmentation, *Mar. Geophys. Res.*, *19*, 457–480.

Pautot, G., C. Rangin, A. Briais, J. Wu, S. Han, H. Li, Y. Lu, and J. Zhao (1990), The axial ridge of the South China Sea: A seabeam and geophysical survey, *Oceanol. Acta*, *13*(2), 129–143.

Purdy, G. M., L. S. L. Kong, G. L. Christeson, and S. C. Solomon (1992), Relationship between spreading rate and the seismic structure of midocean ridges, *Nature*, *355*(6363), 815–817.

Ranero, C. R., and T. J. Reston (1999), Detachment faulting at ocean core complexes, *Geology*, *27*, 983–986.

Reid, I., and H. R. Jackson (1981), Oceanic spreading rate and crustal thickness, *Mar. Geophys. Res.*, *5*(2), 165–172.

Roest, W. R., and S. P. Srivastava (1989), Sea-floor spreading in the Labrador Sea: A new reconstruction, *Geology*, *17*(11), 1000–1003.

Roots, W. D., and S. P. Srivastava (1984), Origin of the marine magnetic quiet zones in the Labrador and Greenland Seas, *Mar. Geophys. Res.*, *6*(4), 395–408.

Sallarès, V., S. Martìnez-Loriente, M. Prada, E. Gràcia, C. Ranero, M.-A. Gutscher, R. Bartolomé, A. Gailler, J. J. Dañobeitia, and N. Zitellini (2013), Seismic evidence of exhumed mantle rock basement at the Gorringe Bank and the adjacent Horseshoe and Tagus abyssal plains (SW Iberia), *Earth Planet. Sci. Lett.*, *365*, 120–131, doi:10.1016/j.epsl.2013.01.021.

Sallarès, V., A. Gailler, M.-A. Gutscher, D. Graindorge, R. Bartolomé, E. Gràcia, J. Dìaz, J. J. Dañobeitia, and N. Zitellini (2011), Seismic evidence for the presence of Jurassic oceanic crust in the central Gulf of Cadiz (SW Iberian margin), *Earth Planet. Sci. Lett.*, *311*(1–2), 112–123, doi:10.1016/j.epsl.2011.09.003.

Sibuet, J., S. Srivastava, and G. Manatschal (2007), Exhumed mantle-forming transitional crust in the Newfoundland-Iberia rift and associated magnetic anomalies, *J. Geophys. Res.*, *112*(B6), B06105, doi:10.1029/2005JB003856.

Sørensen, A. B. (2006), Stratigraphy, structure and petroleum potential of the Lady Franklin and Maniitsoq Basins, offshore southern West Greenland, *Pet. Geosci.*, *12*, 221–234, doi:10.1144/1354-079305-692.

Srivastava, S., K. Louden, S. Chough, D. Mosher, B. D. Loncarevic, P. Mudie, A. de Vernal, and B. MacLean (1989), Results of detailed geological and geophysical measurements at ODP sites 645 in Baffin Bay and 646 and 647 in the Labrador Sea, *Proc. Ocean Drill. Program Sci. Results*, *105*, 891–922.

Srivastava, S., J. Sibuet, S. Cande, W. Roest, and I. Reid (2000), Magnetic evidence for slow seafloor spreading during the formation of the Newfoundland and Iberian margins, *Earth Planet. Sci. Lett.*, *182*, 61–76, doi:10.1016/s0012-821x(00)00231-4.

Srivastava, S. P. (1978), Evolution of the Labrador Sea and its bearing on the early evolution of the North Atlantic, *Geophys. J. R. Astron. Soc.*, *52*, 313–357.

Srivastava, S. P., and C. E. Keen (1995), A deep seismic-reflection profile across the extinct Mid-Labrador sea spreading center, *Tectonics*, *14*(2), 372–389.

Srivastava, S. P., and W. R. Roest (1999), Extent of oceanic crust in the Labrador Sea, *Mar. Pet. Geol.*, *16*, 65–84.

Storey, M., R. A. Duncan, A. K. Pedersen, L. M. Larsen, and H. C. Larsen (1998), 40Ar/39Ar geochronology of the West Greenland tertiary volcanic province, *Earth Planet. Sci. Lett.*, *160*, 569–586.

Suckro, S. K., K. Gohl, T. Funck, I. Heyde, A. Ehrhardt, B. Schreckenberger, J. Gerlings, V. Damm, and W. Jokat (2012), The crustal structure of southern Baffin Bay: Implications from a seismic refraction experiment, *Geophys. J. Int.*, *190*, 37–58, doi:10.1111/j.1365-246X.2012.05477.x.

Talwani, M., and O. Eldholm (1977), Evolution of the Norwegian-Greenland sea, *Geol. Soc. Am. Bull.*, *88*, 969–999.

Talwani, M., J. Lamar Worzel, and M. Landisman (1959), Rapid gravity computations for two-dimensional bodies with application to the Mendocino submarine fracture zone, *J. Geophys. Res.*, *64*(1), 49–59.

Tucholke, B. E., and J. Lin (1994), A geological model for the structure of ridge segments in slow spreading ocean crust, *J. Geophys. Res.*, *99*, 11,937–11,958.

Tucholke, B. E., J. Lin, and M. C. Kleinrock (1998), Megamullions and mullion structure defining oceanic metamorphic core complexes on the Mid-Atlantic Ridge, *J. Geophys. Res.*, *103*, 9857–9866.

Tucholke, B. E., M. D. Behn, W. R. Buck, and J. Lin (2008), Role of melt supply in oceanic detachment faulting and formation of megamullions, *Geology*, *36*(6), 455–458, doi:10.1130/G24639A.1.

Uenzelmann-Neben, G., W. Jokat, H. Miller, and S. Steinmetz (1992), The Aegir ridge: Structure of an extinct spreading axis, *J. Geophys. Res.*, *97*(B6), 9203–9218.

Van Avendonk, H. J. A., A. J. Harding, A. Orcutt, and W. S. Holbrook (2001), Hybrid shortest path and ray bending method for traveltime and raypath calculations, *Geophysics*, *66*, 648–653, doi:10.1190/1.1444955.

Van Avendonk, H. J. A., D. J. Shillington, W. S. Holbrook, and M. J. Hornbach (2004), Inferring crustal structure in the Aleutian island arc from a sparse wide-angle seismic data set, *Geochem. Geophys. Geosyst.*, *5*, Q08008, doi:10.1029/2003GC000664.

Watremez, L., K. W. H. Lau, M. R. Nedimovic, and K. E. Louden (2015), Traveltime tomography of a dense wide-angle profile across Orphan Basin, *Geophysics*, *80*(3), B69–B82, doi:10.1190/geo2014-0377.1.

Watt, W. (1969), The coast-parallel dike swarm of southwest Greenland in relation to the opening of the Labrador Sea, *Can. J. Earth Sci.*, *6*, 1320–1321.

White, R. S., D. McKenzie, and R. K. O'Nions (1992), Ocean crustal thickness from seismic measurements and rare Earth elements inversions, *J. Geophys. Res.*, *97*, 19,683–19,716.

Wu, Y., K. E. Louden, T. Funck, H. R. Jackson, and S. A. Dehler (2006), Crustal structure of the central Nova Scotia margin off Eastern Canada, *Geophys. J. Int.*, *166*, 878–906, doi:10.1111/j.1365-246X.2006.02991.x.

Zelt, C., and P. Barton (1998), Three-dimensional seismic refraction tomography: A comparison of two methods applied to data from the Faeroe Basin, *J. Geophys. Res.*, *103*(B4), 7187–7210.

Zelt, C., and D. Forsyth (1994), Modeling wide-angle seismic data for crustal structure: Southeastern Grenville Province, *J. Geophys. Res.*, *99*, 11,687–11,704.

Zelt, C. A., and R. B. Smith (1992), Seismic traveltime inversion for 2-D crustal velocity structure, *Geophys. J. Int.*, *108*(1), 16–34.

Zhang, J., and M. N. Toksøz (1998), Nonlinear refraction traveltime tomography, *Geophysics*, *63*, 1726–1737, doi:10.1190/1.1444468.